J. Fluid Mech. (1993), *vol.* 254, *pp.* 151–181

A numerical nonlinear analysis of the flow around two- and three-dimensional partially cavitating hydrofoils

By SPYROS A. KINNAS AND NEAL E. FINE

Department of Ocean Engineering, Massachusetts Institute of Technology, Cambridge, MA 02139, USA

(Received 8 October 1991 and in revised form 5 February 1993)

The partially cavitating two-dimensional hydrofoil problem is treated using nonlinear theory by employing a low-order potential-based boundary-element method. The cavity shape is determined in the framework of two independent boundary-value problems; in the first, the cavity length is specified and the cavitation number is unknown, and in the second the cavitation number is known and the cavity length is to be determined. In each case, the position of the cavity surface is determined in an iterative manner until both a prescribed pressure condition and a zero normal velocity condition are satisfied on the cavity. An initial approximation to the nonlinear cavity shape, which is determined by satisfying the boundary conditions on the hydrofoil surface rather than on the exact cavity surface, is found to differ only slightly from the converged nonlinear result.

The boundary element method is then extended to treat the partially cavitating three-dimensional hydrofoil problem. The three-dimensional kinematic and dynamic boundary conditions are applied on the hydrofoil surface underneath the cavity. The cavity planform at a given cavitation number is determined via an iterative process until the thickness at the end of the cavity at all spanwise locations becomes equal to a prescribed value (in our case, zero). Cavity shapes predicted by the present method for some three-dimensional hydrofoil geometries are shown to satisfy the dynamic boundary condition to within acceptable accuracy. The method is also shown to predict the expected effect of foil thickness on the cavity size. Finally, cavity planforms predicted from the present method are shown to be in good agreement to those measured in a cavitating three-dimensional hydrofoil experiment, performed in MIT's cavitation tunnel.

1. Introduction

Modelling cavitating or free streamline flows has been the subject of much research for at least a century. Originally, free streamline flows were used to model the separated flow in the wake of bluff bodies to provide estimates for bluff body drag. Since then, in many engineering applications – particularly hydrofoils, liquid pumps and marine propellers – cavitation has been a subject of research because it is an undesirable phenomenon. This is due mainly to the detrimental effects (e.g. structural failure, corrosion, and noise radiation) of collapsing vapour bubbles. In the past, the goal in the hydrodynamic design of all these water devices was to avoid cavitation by shaping the geometry appropriately so that the pressure everywhere is higher than the cavitation inception pressure. However, recent marine applications have seen an increasing demand for higher boat speeds and lower fuel consumption, with the result

that hydrofoil or propeller cavitation is often unavoidable. It has hence become the task of the hydrodynamicist to predict the cavitation characteristics of these lifting surfaces and propulsors at the design stage, so that the worst characteristics may be avoided in an appropriate range of ship speed, r.p.m. or propeller thrust. Computational tools for the reliable prediction of hydrofoil and propeller cavitation are therefore in high demand. In particular, a type of cavitation that is very common on marine propellers is *sheet* cavitation, in which a distinct thin vapour bubble is attached to the blade surface. Other types of cavitation which also occur include cloud and bubble cavitation. However, this work addresses the computational analysis of sheet hydrofoil cavitation only.

The main difficulty in the analysis of cavitating flows arises from the need to determine the free streamline (the cavity surface) on which the pressure is prescribed. The fact that the location of a portion of the flow boundary is unknown is one contribution to the nonlinearity of the problem. In addition, there has been diversity in the methods of simulating the flow at the end of the cavity, whose nature is usually two-phase and turbulent. Several *cavity closure models* have been devised to represent this region, and among the most popular models have been those of Riabouchinsky, the re-entrant jet, the spiral vortex and the open wake. A description of these and other models may be found in Tulin (1964).

Cavitating flows in two-dimensions were first addressed by employing the hodograph technique, as introduced by Helmholtz, Kirchoff and Levi-Civita see Birkhoff & Zarantonello (1957). However, due to the difficulty of applying the hodograph technique to general shape geometries, only a few have been treated analytically (e.g. flat plate, circular and wedge geometries). This technique was extended numerically to treat arbitrary geometries by Wu & Wang (1964) and later applied by Furuya (1975*a*) to the analysis of supercavitating hydrofoils in the presence of a free surface.

The linear theory for the analysis of the cavitating flow around two-dimensional hydrofoils at zero or non-zero cavitation number was introduced by Tulin (1953, 1955). Linear theory was first applied to partially cavitating hydrofoils independently by Acosta (1955) and Geurst & Timman (1956). The linear cavity theory, which closely resembles the classical thin-wing theory, assumes thin cavity and foil thickness relative to the foil chord length and, as a result, simplifies the dynamic boundary condition from the requirement of constant total velocity to that of constant horizontal perturbation velocity. This boundary condition is applied, together with the linearized wetted surface kinematic boundary condition, on a projection of the hydrofoil surface on the free-stream axis. Linear cavity theory has been applied by several researchers for the analysis of partial and supercavitating flows around special and general shape two-dimensional hydrofoil geometries. A list of references which address the application of linear cavity theory may be found in Tulin & Hsu (1980) or Kinnas (1991).

The flow around cavitating finite-span hydrofoils (also called three-dimensional hydrofoils in this work) was first treated in a stripwise sense with the three-dimensional flow effects introduced by matching the inner solution (in either linear or nonlinear theory) with the solution from lifting-line theory in the outer domain. This approach was used to study supercavitating hydrofoils by Nishiyama (1970), Leehey (1971) and Furuya (1975*b*), partially cavitating hydrofoils by Uhlman (1978), and partially or supercavitating hydrofoils in unsteady flow by Van Houten (1982). However, this method is valid only for high-aspect-ratio hydrofoils and its accuracy deteriorates at the tips of the hydrofoil. The complete three-dimensional flow effects, in the context of linear cavity theory, were included in the analysis of supercavitating three-dimensional hydrofoils in unsteady flow by Widnall (1966), who employed a numerical pressure

doublet and source lifting-surface technique. Jiang & Leehey (1977) applied instead a discrete vortex and source lattice lifting-surface technique, and also introduced an iterative scheme for determining the cavity planform until a uniform cavitation number was achieved at all spanwise locations. This technique was then applied to the analysis of unsteady propeller cavitation by Lee (1979) and Breslin *et al.* (1982), who also introduced the ability to treat mixed cavity patterns in partial cavitation and supercavitation.

Owing to the success of thin-wing theory in the analysis of fully wetted flows, one would assume that linear cavity theory would be appropriate for analysing hydrofoil or propeller sheet cavitation. However, a serious defect of the linear theory arises in the case of partially cavitating flows around hydrofoils with rounded leading edges. In particular, linear theory predicts that the cavity extent and volume should increase with increasing thickness provided that the flow conditions remain the same. On the other hand, the short-cavity theory of Tulin & Hsu (1980) and the numerical nonlinear surface vorticity method developed by Uhlman (1987), predict that the cavity size should decrease with increasing thickness. In addition, it is known from experimental evidence that increasing the leading-edge radius delays or reduces leading-edge cavitation. This defect of the linear cavity theory has recently been corrected by Kinnas (1991) who introduced the nonlinear *leading-edge correction* to account for the breakdown of the linear cavity solution in the vicinity of a round leading edge. This was accomplished by modifying the linearized dynamic boundary condition to one of varying horizontal perturbation velocity rather than constant velocity as required by the conventional linear cavity theory. The nonlinear blade thickness effects have also been included in the linearized method for the analysis of unsteady propeller cavitation, mentioned previously, by implementing the leading-edge correction locally at planes normal to the blade leading edge (Kerwin *et al.* 1986).

The application of numerical methods for the nonlinear analysis of axisymmetric cavity flows was introduced by Brennen (1969) who utilized a finite-difference approach. However, since the flow is being treated as potential, boundary-element methods (BEMs) are more suitable. Various velocity-based BEMs have been applied for the analysis of the flow around two- and three-dimensional partially and supercavitating hydrofoils. These include methods by Pellone & Rowe (1981) for supercavitating three-dimensional hydrofoils, by Uhlman (1987, 1989) for partially and supercavitating two-dimensional hydrofoils, and by Lemonnier & Rowe (1988), for partially cavitating two-dimensional hydrofoils. In each of these BEMs, the panels are placed on the cavity boundary, whose shape is determined by an iterative process which terminates when both the kinematic and the dynamic boundary conditions are satisfied. More recently, a potential-based boundary-element method (i.e. one based on Green's third identity for the perturbation potential) was developed by Kinnas & Fine (1991) for the nonlinear analysis of the flow around partially and supercavitating two-dimensional hydrofoils. This method, when applied to partially cavitating hydrofoils (with the cavity length known and the cavitation number unknown) has been found to converge to the final cavity shape with fewer iterations than velocity-based BEMs. In particular, it has been found that the first step in the iterative method, in which the dynamic boundary condition is satisfied on the hydrofoil surface beneath the cavity, predicts a cavity shape which is very close to the correct nonlinear shape.

In the present work, first the potential-based BEM is extended to predict the cavity extent and shape for two-dimensional partially cavitating hydrofoils at given cavitation number. The method is then applied in three dimensions, where the fully three-dimensional boundary conditions are satisfied on the foil surface beneath the cavity.

2. Partially cavitating two-dimensional hydrofoil

2.1. *Formulation*

Consider a partially cavitating hydrofoil of chord length $c = 1$ subject to a uniform inflow, U_∞, with ambient pressure, p_∞, as shown in figure 1. The cavity detaches from the foil surface at point D ($x = l_D$) on the suction side of the foil and rejoins the foil at point L ($x = l \equiv$ cavity length). The pressure on the cavity surface is constant and equal to p_c between D and T. In the transition zone between T and L a cavity termination model is imposed, as will be described later in this section. The x-coordinate of the point T, x_T, is defined in terms of the parameter λ from the expression $x_T = (1-\lambda)l$.

Assuming that the fluid is inviscid and incompressible, and that the resulting flow is irrotational, we can express the total velocity flow field, $\boldsymbol{q}$, in terms of either the total potential, Φ, or the perturbation potential, ϕ, as

$$\boldsymbol{q} = \nabla\Phi = U_\infty + \nabla\phi. \tag{1}$$

The total and perturbation potentials are related as follows:

$$\phi(x,y) = \Phi(x,y) - \Phi_{in}(x,y), \tag{2}$$

where the inflow velocity potential Φ_{in} corresponds to the uniform inflow of magnitude U_∞ at an angle of attack α:

$$\Phi_{in}(x,y) = U_\infty(x\cos\alpha + y\sin\alpha). \tag{3}$$

The perturbation potential ϕ will satisfy Laplace's equation in the domain outside the cavity and hydrofoil

$$\nabla^2\phi = 0. \tag{4}$$

In addition, the following boundary conditions on ϕ are applied.

(i) Kinematic boundary condition: the flow is required to be tangent to the wetted hydrofoil surface as well as to the cavity surface. If $\hat{\boldsymbol{n}}$ is the unit normal to the hydrofoil or cavity surface directed into the fluid domain, then the kinematic boundary condition is given by

$$\frac{\partial\phi}{\partial n} = -\frac{\partial\Phi_{in}}{\partial n} = -\nabla\Phi_{in}\cdot\hat{\boldsymbol{n}} = -U_\infty\cdot\hat{\boldsymbol{n}} \tag{5}$$

on the wetted foil and cavity surface.

(ii) Dynamic boundary condition on the cavity: the pressure is required to be constant on the cavity surface from D to T and equal to p_c. Applying Bernoulli's equation and the definition of the cavitation number, σ

$$\sigma = \frac{p_\infty - p_c}{\frac{1}{2}\rho U_\infty^2}, \tag{6}$$

the magnitude of the total velocity on the cavity, q_c, is found to be constant:

$$q_c = U_\infty(1+\sigma)^{\frac{1}{2}}. \tag{7}$$

(iii) Kutta condition:

$$\nabla\phi = \text{finite; at the trailing edge.} \tag{8}$$

(iv) Condition at infinity:

$$\nabla\phi \to 0 \text{ at infinity.} \tag{9}$$

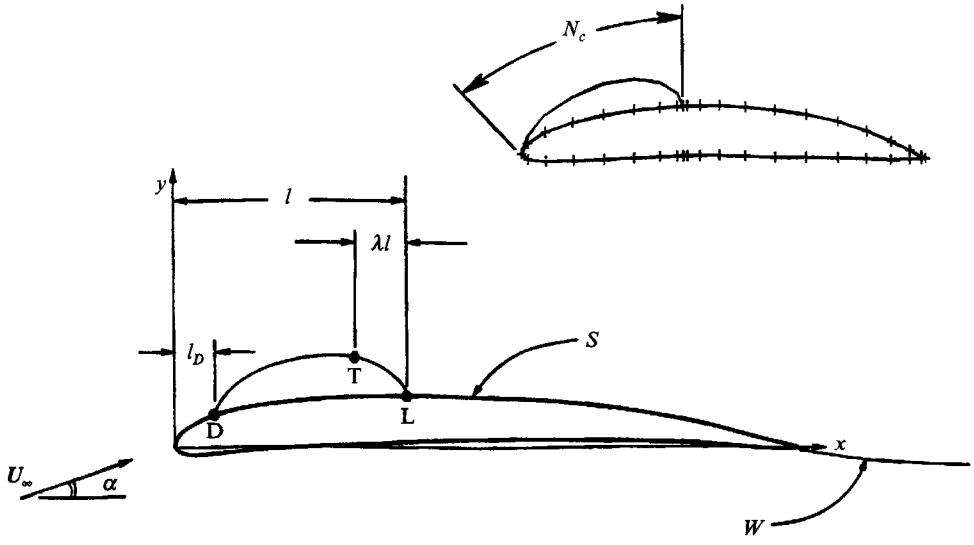

FIGURE 1. Partially cavitating two-dimensional hydrofoil. The panel arrangement for $N = 40$ and $N_c = 8$ is also shown.

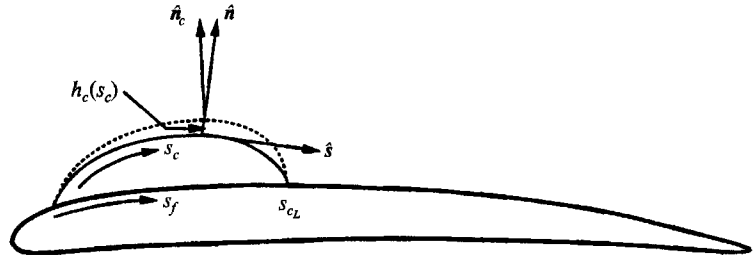

FIGURE 2. Cavity shapes at the current and next iteration.

(v) Cavity termination model: a termination model must be applied at the end of the cavity. It may be chosen from a list of existing models, such as the Riabouchinsky model, the re-entrant jet model, the spiral vortex model, or the open viscous wake model. In the present work, we employ a cavity termination model in which the velocity (i.e. pressure) in the transition zone (between T and L in figure 1) departs from its constant value on the cavity according to a prescribed law (Lemonnier & Rowe 1988). In particular, we employ the following algebraic law for the velocity on the cavity:

$$\frac{\partial \phi}{\partial s_c} + \frac{\partial \Phi_{in}}{\partial s_c} = q_c[1 - f(s_f)], \tag{10}$$

where s_c, as shown in figure 2, is the arclength of the cavity and $f(s_f)$ is

$$f(s_f) = \begin{cases} 0 & s_f < s_T \\ A\left[\dfrac{s_f - s_T}{s_L - s_T}\right]^\nu, & s_T \leqslant s_f \leqslant s_L. \end{cases} \tag{11}$$

Here, s_f is the arclength of the foil beneath the cavity measured from the cavity leading edge, and A ($0 < A < 1$) and ν ($\nu > 0$) are arbitrary constants. In the future, ν, λ and

A will be taken from experimental information at the trailing edge of the cavity. The effect of λ and ν on the cavity shape has been shown in Kinnas & Fine (1991). Note, however, that the current pressure law differs slightly from the one in that paper, in that the velocity in the transition zone is attenuated to a fraction of the cavity velocity.

In addition to the above boundary conditions, we will assume that the cavity height vanishes at its trailing edge (see §5 for discussion of this assumption):

$$h(s_L) = 0. \tag{12}$$

For the chosen cavity termination model, a given cavity detachment location l_D and cavity length l, equation (4) can be solved subject to the conditions (5), (8), (9), (10) and (12). The cavity shape and the corresponding cavitation number will then be determined from the solution.

2.2. *Cavity shape for fixed cavity length*

The boundary-value problem described in the previous section is most readily solved in the case where the cavity length, as well as its point of detachment, are known. The cavity shape and the corresponding cavitation number are unknown and will be determined by applying a potential-based boundary-element method. The method is described in detail in Kinnas & Fine (1991), but a condensed description is included here for completeness.

The perturbation potential, ϕ, must satisfy Green's formula, a Fredholm integral equation of the second kind, on the foil and cavity:

$$\pi\phi_p = \int_S \left[-\phi \frac{\partial \ln R}{\partial n} + \frac{\partial \phi}{\partial n} \log R \right] \mathrm{d}S - \int_W \Delta\phi_w \frac{\partial \ln R}{\partial n} \mathrm{d}S \quad \text{on} \quad S, \tag{13}$$

where S is the surface of the wetted foil or the cavity and W is the surface of the wake, as shown in figure 1. R is the distance from the surface element $\mathrm{d}S$ to the point p. $\Delta\phi_w$ is the potential jump in the wake.

On the wetted part of the foil, the value of $\partial\phi/\partial n$ is known and given by (5). On the cavity, an expression for ϕ may be found by integrating (10):

$$\phi(s_c) = \phi(0) - \Phi_{in}(s_c) + \Phi_{in}(0) + q_c \int_0^{s_c} [1 - f(s_f)] \, \mathrm{d}s_c. \tag{14}$$

To numerically invert the integral equation (13), subject to the boundary conditions (5) and (14), the cavity and foil surfaces are discretized into N straight panels whose vertices lie on S. N_c of these panels are located on the cavity, while the remainder, $N_w = N - N_c$, lie on the wetted part of the foil (see figure 1). A full cosine spacing of the panel boundaries is implemented between the foil leading edge and the cavity trailing edge, and between the cavity trailing edge and the foil trailing edge, in order to concentrate more panels where sharp velocity gradients are expected. The continuous source and dipole distributions on each panel are approximated by constant strength distributions. Equation (13) is applied, in its discretized form, at the midpoints of the panels. The Kutta condition (8) is numerically implemented by employing Morino's condition (Morino & Kuo 1974):

$$\Delta\phi_w = \phi_T^+ - \phi_T^-, \tag{15}$$

where ϕ_T^+ and ϕ_T^- are the potentials at the upper and lower trailing-edge panels, respectively.

The unknowns to be determined from the N equations will be: N_w dipole strengths, ϕ, at the panels which represent the wetted part of the foil; N_c source strengths, $\partial\phi/\partial n$, at the panels which represent the cavity; the cavity velocity, q_c, or equivalently (via (7)), the cavitation number σ. Note that there are a total of $N+1$ unknowns to be determined.

The cavity surface, and thus s_c, is not known and in the present method will be determined iteratively. As a first iteration, the cavity panels are placed on the foil underneath the cavity. At each successive iteration the edges of the cavity panels are relocated on the updated cavity surface, which was computed at the end of the previous iteration. The cavity height (taken normal to the present iteration cavity surface, as shown in figure 2) is h_c and it represents the amount by which the updated cavity surface has to be corrected. It can be shown that the following relationship is valid up to first order in h_c (Kinnas & Fine 1991):

$$q_c[1-f(s_f)]\frac{\mathrm{d}h_c}{\mathrm{d}s_c}=\frac{\partial\phi}{\partial n}+\frac{\partial\Phi_{in}}{\partial n}. \tag{16}$$

Combining (12) and (16), we arrive at the cavity closure condition:

$$\int_0^{s_{c_L}}\frac{\partial\phi}{\partial n}\frac{\mathrm{d}s_c}{1-f(s_f)}=-\int_0^{s_{c_L}}\frac{\partial\Phi_{in}}{\partial n}\frac{\mathrm{d}s_c}{1-f(s_f)}, \tag{17}$$

where s_{c_L} is the total arclength of the cavity surface, as shown in figure 2.

Equation (17) provides the additional equation needed to determine the $N+1$ unknowns. Once the solution is found and $\partial\phi/\partial n$ is known, the incremental cavity thickness h_c can be determined by integrating (16). The new position of the cavity surface and the new arclength, s_c, can then be determined and used in the next iteration.

The value of $\phi(0)$ in (14) corresponds to the value of the perturbation potential at the detachment point of the cavity, labelled D in figure 1. $\phi(0)$ is not known and in the present numerical scheme is expressed via a cubic extrapolation in terms of the unknown potentials on the wetted panels in front of the cavity.

The numerical validation of the method is addressed extensively in Kinnas & Fine (1991). An application of the method to a particular case and the sequence of the cavity shapes and the corresponding cavitation numbers at different iterations are shown in figure 3. The cavity shape and cavitation number appear to be converged by the end of the second iteration, while even the results from the first iteration are very close to the converged ones. It has been shown in Kinnas & Fine (1991) that the convergence of the cavity shape predicted by the present method is much quicker than that of Uhlman's (1987) velocity-based boundary-element method.

2.3. *Cavity shape for fixed cavitation number*

The boundary-value problem considered in the previous section involved a two-dimensional cavity of known length and unknown cavitation number. A more natural problem, however, is the so-called 'direct problem', in which we have to determine the cavity extent and shape for given cavitation number. Such a problem has, for example, to be solved at each spanwise location of a three-dimensional hydrofoil (or propeller) to determine the three-dimensional cavity extent and shape at a given cavitation number, as will be described in §3.

One obvious way of solving the direct problem in two dimensions is to solve the full nonlinear fixed-length problem at several cavity lengths, l, and then interpolate for the

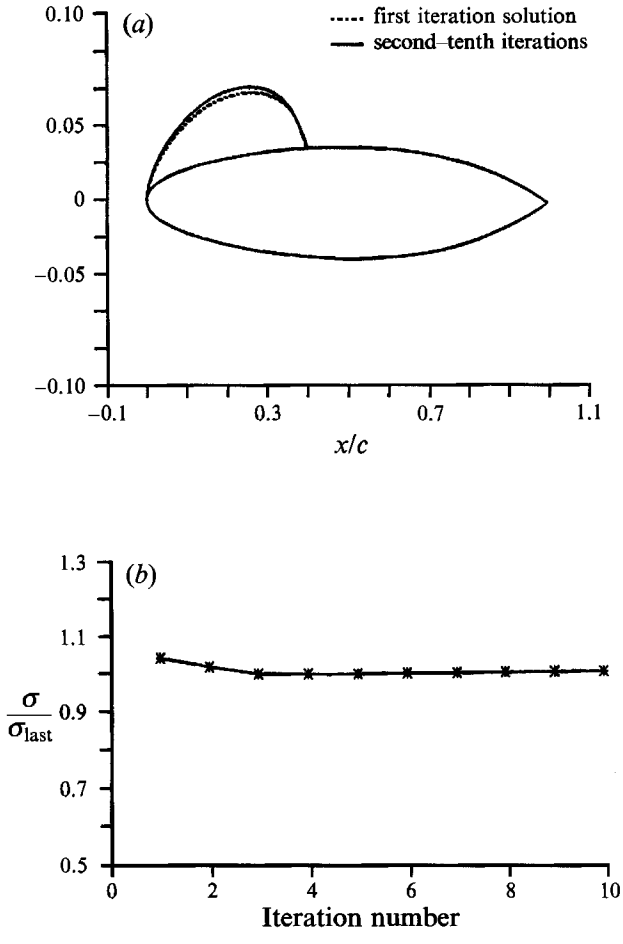

FIGURE 3. Convergence of (*a*) cavity shape and (*b*) cavitation number with number of iterations for a NACA16006 hydrofoil at $\alpha = 4°$ and for fixed cavity length $l = 0.4$, $l_D = 0$, $\lambda = 0.1$, $\nu = 1.0$, $A = 0.5$.

correct l at the given σ. However, solving the nonlinear problem many times is expensive, even for the present panel method in which the regridding of the cavity surface is rather minimal. Solving the problem in this manner would raise the computing time substantially, especially when applied to the prediction of unsteady hydrofoil or propeller cavitation. Our objective is to develop a general procedure for determining the nonlinear cavity shape requiring the least regridding. The proposed algorithm is described next.

2.3.1. *Cavity shape – first iteration – the split-panel technique*

For given cavitation number, σ, we start with a guess for the cavity length, l. The foil and cavity are then discretized with the cavity panels located on the foil underneath it, as was done in the first iteration of the fixed-cavity-length problem. This problem, however, differs from that described in the previous section in that the cavitation number is known and thus its value is used in the expression for the potential on the cavity surface given by (14). Green's formula, (13), is still applied at the control points, but now there is no need to apply the closure condition (12), since the number of

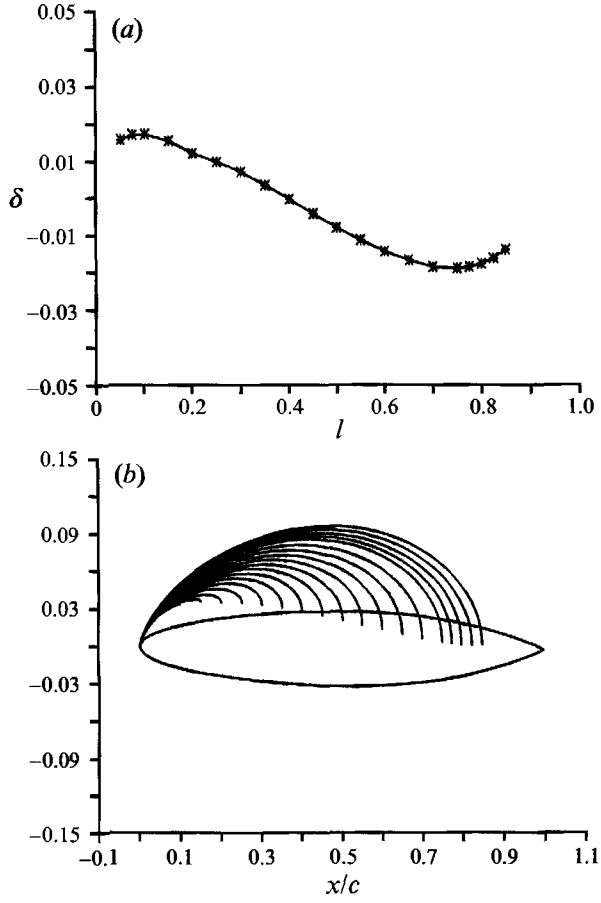

FIGURE 4. NACA16006 hydrofoil at $\alpha = 4°$ and fixed cavitation number $\sigma = 1.097$ (corresponding to the correct length $l = 0.4$). (*b*) The predicted cavity shapes for different guesses of l, (*a*) the resulting behaviour of δ *vs.* l. The panels representing the cavity are located on the foil underneath it (first iteration).

unknowns is reduced by one. Nonetheless, as expected, the cavity will not close at its trailing edge unless the cavity length corresponds to the prescribed σ. The thickness of the cavity at its end, δ, can be determined by integrating (16):

$$\delta(l;\sigma) \equiv h_c(s_{c_L}) = \frac{1}{q_c}\int_0^{s_{c_L}} \left[\frac{\partial \Phi_{in}}{\partial n} + \frac{\partial \phi}{\partial n}\right] \frac{\mathrm{d}s_c}{1 - f(s_f)}, \tag{18}$$

where ϕ corresponds to the solution of the direct problem at cavity length l. Note that $s_c = s_f$ since within this phase the cavity panels are located on the foil surface.

In figure 4(*b*) the cavity shapes are shown for a NACA16006 hydrofoil at an angle of attack of 4° and for different cavity length guesses. The cavitation number for each is $\sigma = 1.097$, which corresponds to the cavity length $l = 0.4$ from the first iteration of the fixed-length solution of §2.2. Notice that the cavity closes for the guess $l = 0.4$, as expected. Figure 4(*a*) shows the openness of the cavity at its trailing edge, δ, plotted versus the cavity length, l. Notice that there appears to be only one solution for $\delta = 0$, provided that (unstable) cavity lengths greater than $l \approx 0.75$ are not allowed.

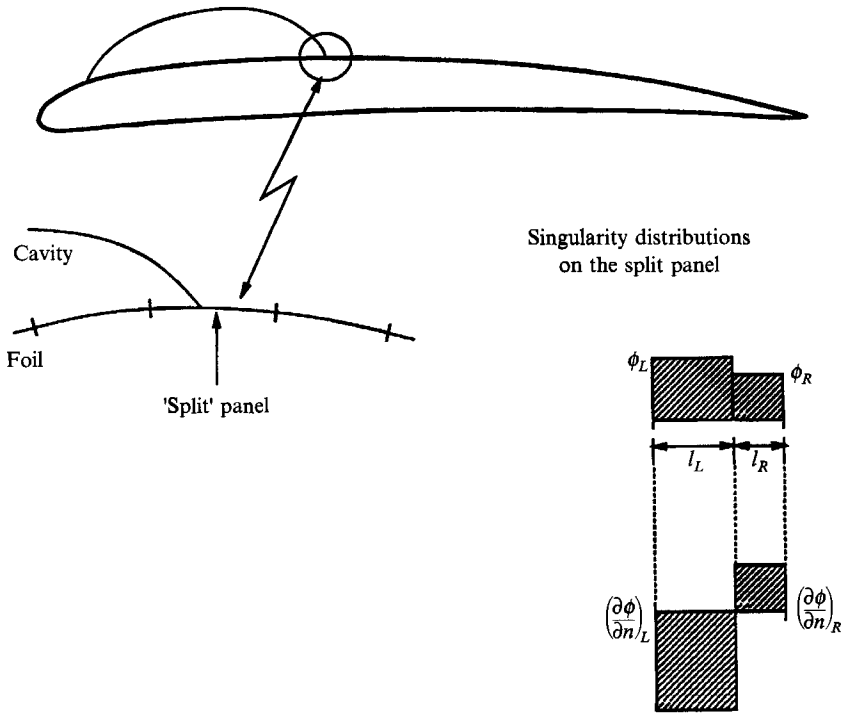

FIGURE 5. Depiction of the split-panel technique in two dimensions.

A Newton–Raphson (secant method) technique is applied to determine the cavity length l from the solution of the equation

$$\delta(l;\sigma) = 0. \tag{19}$$

In order to avoid unstable cavities, only the solution with the shortest cavity length, for which $\mathrm{d}\delta/\mathrm{d}l < 0$, is accepted. The method typically takes 3 or 4 iterations to converge (with $|\delta| \leqslant 5\times10^{-4}$) to the correct cavity length.

For each new guess of the cavity length, the foil may be repanelled to maintain cosine spacing of the panel boundaries between the cavity trailing edge and the foil leading and trailing edges. This simplifies the Newton–Raphson iterations, since the trailing edge of the cavity always coincides with a panel boundary. However, as mentioned previously, repanelling would be very expensive and thus not desirable at this stage of the three-dimensional solution. We turn, then, to an alternative in which the panelling does not change, but the cavity trailing edge is not required to coincide with a panel boundary. Thus, in this method there is a single panel, located at the trailing edge of the cavity, which is partly cavitating and partly wetted (see figure 5). This panel will be referred to as the 'split' panel, since it is split by the cavity trailing edge. Green's formula (13) is not applied on the split panel. The source and dipole strengths on the split panel are defined as the weighted average of the strengths on the cavitating part of the panel and those on the wetted part of the panel, as follows:

$$\phi = \frac{\phi_L l_L + \phi_R l_R}{l_L + l_R}, \quad \frac{\partial\phi}{\partial n} = \frac{(\partial\phi/\partial n)_L l_L + (\partial\phi/\partial n)_R l_R}{l_L + l_R} \quad \text{on the split panel,} \tag{20}$$

where the subscript L denotes the left side of the split panel and the subscript R denotes the right side. As shown in figure 5, l_L and l_R are the lengths of the left and right sides

of the split-panel, respectively. The quantities $(\partial\phi/\partial n)_R$ and ϕ_L are known from the boundary conditions, (5) and (14). The quantities $(\partial\phi/\partial n)_L$ and ϕ_R are unknown, but may be defined as extrapolations of the unknowns on adjacent panels (similar to the definition of $\phi(0)$ in (14)). ϕ_R is defined by a four-point cubic extrapolation, while $(\partial\phi/\partial n)_L$ is defined by a one-point extrapolation assuming that $(\partial\phi/\partial n)(s)$ is characterized by a square-root singularity at the trailing edge of the cavity. Note that both the number of unknowns and the number of equations have been reduced by one.

The first iteration cavity length and shape have thus been found by two methods: one in which the foil is repanelled after each Newton–Raphson iteration and the other involving the split-panel technique just described. The results from these two methods and for the same total number of panels N have been compared for several cavitation numbers and the split-panel method has been found to be equally robust and to converge to the same solution with a comparable number of iterations as the method of repanelling. The split-panel technique, however, allows the treatment of a continuous spectrum of cavity lengths (i.e. cavitation numbers) by using only one panelling arrangement. Moreover, in three dimensions, as will be described in §3, the split-panel technique allows a smoother discretization of the trailing edge of the cavity planform in the spanwise direction.

2.3.2. *Regridding*

It is not immediately clear how to proceed from the first iteration cavity length to a converged nonlinear cavity length. If we 'build on' the resulting cavity by moving the panels which represent the cavity from the foil surface to the newly computed cavity surface and apply (13) there for the given cavitation number, then the result will be a cavity which does not close. In fact, since we know from experience with the fixed-length solution that the nonlinear σ is always less than the first iteration σ, we can predict that the first iteration cavity is too long. Therefore, building on the first iteration cavity usually results in a cavity for which $\delta < 0$. By trimming off the end of the cavity which lies inside the foil, the cavity length may be shortened and another iteration may be built on the resulting cavity shape. Repeating this procedure will eventually lead to the nonlinear cavity shape. Unfortunately, the convergence of this scheme has been found to be very slow.

An accelerated scheme has been developed which takes advantage of the fact that the difference between the cavitation numbers from the first and the converged iterations with fixed cavity length, l, behaves smoothly with l. With σ being the given cavitation number, the proposed algorithm is as follows:

(i) solve the cavity problem (first iteration) with fixed cavitation number $\sigma_0 = \sigma$ to find the corresponding cavity length l_0;

(ii) solve the cavity problem with fixed cavity length l_0 for K iterations (i.e. regridding) and find the converged value of the cavitation number, σ_0';

(iii) define a new cavitation number, $\sigma_1 = \sigma_0 + (\sigma_0 - \sigma_0')$;

(iv) solve the cavity problem (first iteration) with fixed cavitation number σ_n and find the correct cavity length l_n $(n \geqslant 1)$;

(v) solve the cavity problem with fixed cavity length l_n for K iterations, and find the converged value of the cavitation number, σ_n' $(n \geqslant 1)$;

(vi) apply a Newton–Raphson (secant) iterative solution for $\sigma_n' - \sigma = 0$, and find a new cavitation number, σ_{n+1};

(vii) repeat steps iv, v, and vi until $\sigma_n' = \sigma$ to within a preset tolerance.

Figure 6 shows the first and last iterations of an example in which the preset tolerance was set to $(\sigma_n' - \sigma)/\sigma \leqslant 0.01$. Convergence to this tolerance took only one

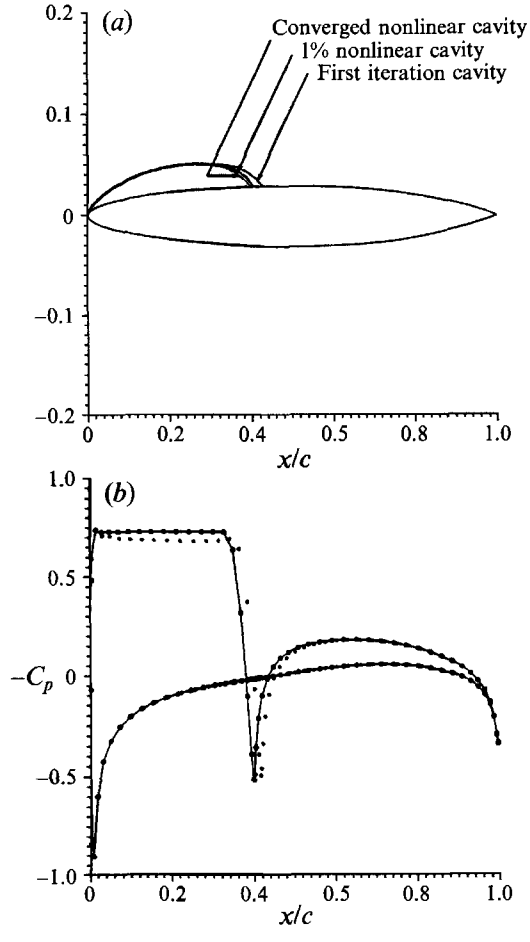

FIGURE 6. NACA16006 foil at $\alpha = 3°$, $\lambda = 0.1$, $\nu = 1.0$, $A = 0.50$, $\sigma = 0.731$, $l_D = 0$. (*a*) The first and last iterations in the convergence to the nonlinear cavity length for given cavitation number, along with the converged cavity shape. The 1% nonlinear cavity is the final iteration, for which $(\sigma_n' - \sigma)/\sigma \leqslant 0.01$. (*b*) A comparison of the pressure distribution from the nonlinear cavity solution (solid line) to that from the fully wetted analysis of the cavities from the first iteration (asterisks) and last iteration (circles).

Newton–Raphson iteration. Since the nonlinear cavitation number at each cavity length was found by iterating twice ($K = 2$), the total number of regriddings for this case was equal to 4. Included in figure 6 is the converged nonlinear cavity (known, since $\sigma = 0.731$ was chosen to correspond to the converged cavity solution with fixed length $l = 0.4$). Also shown in figure 6 is the pressure distribution on the foil and cavity from the converged nonlinear solution (plotted with a solid curve). Superimposed on this curve are two pressure distributions which resulted from an independent fully wetted analysis (Kerwin *et al.* 1987) of a modified foil consisting of the foil and cavity from the first iteration (plotted with asterisks) and the last iteration (plotted with open circles). Note that the pressure distribution (resulting from the fully wetted analysis) on the cavity from the last iteration satisfies the imposed dynamic boundary condition, and even the pressure distribution on the cavity from the first iteration comes very close to satisfying the condition.

Figure 7 shows a comparison of cavity solutions from various methods.

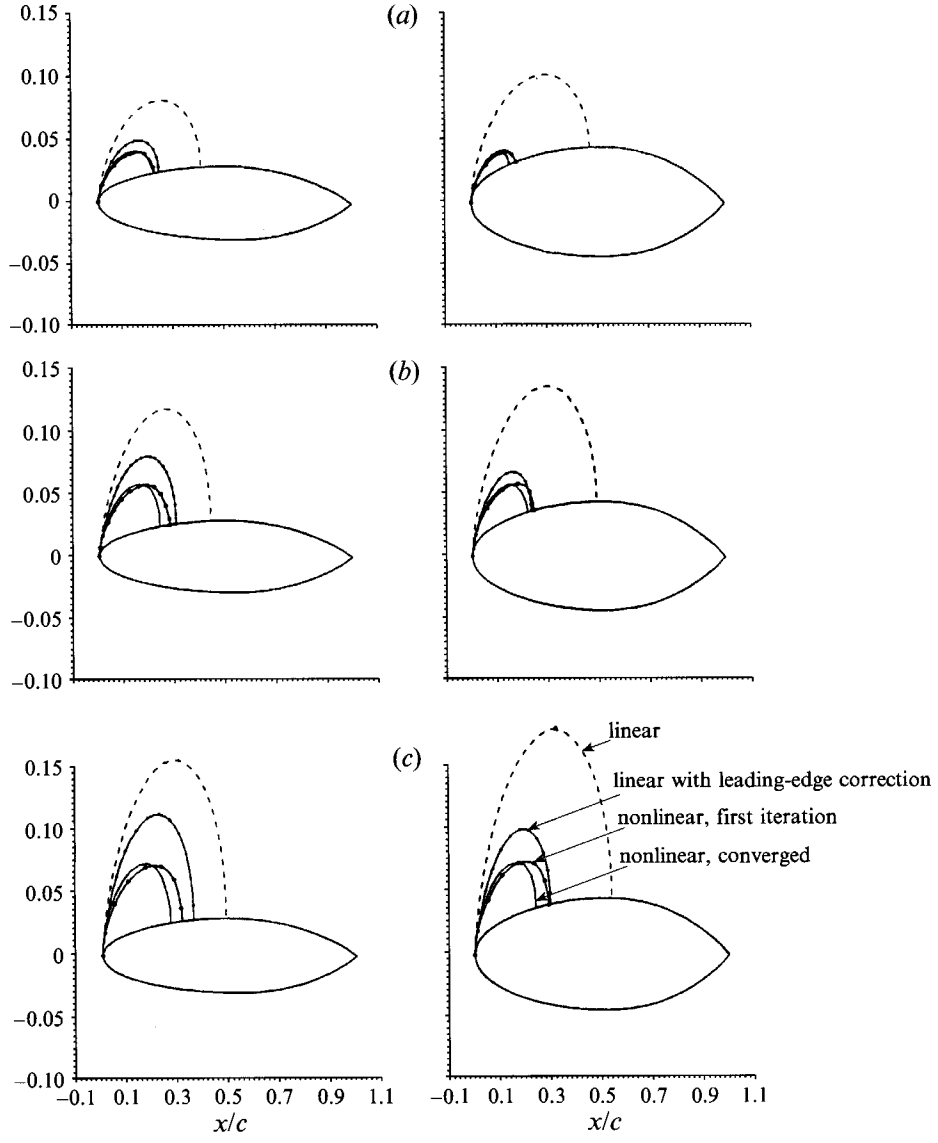

FIGURE 7. Comparison of cavity shapes predicted from different methods for a NACA-16 foil at (*a*) $\alpha = 4°$, (*b*) 6° and (*c*) 8°, and $t/c = 0.06$ (left), and 0.09 (right); t is the maximum thickness of the hydrofoil. The ratio α/σ is kept fixed and equal to 0.055. Detachment at $l_D(y) = 0$. ---, Linear; -●-●-●-, linear with leading-edge correction; -○-○-○-, nonlinear, first iteration; ——, nonlinear, converged.

Superimposed are cavities from linear theory, linear theory with leading-edge corrections (Kinnas 1991), the first iteration of the present method, and the converged nonlinear result. Results are shown for three angles of attack and two thickness-to-chord ratios.

The following may be concluded by studying figures 6 and 7. First, the linear theory substantially overpredicts the converged nonlinear cavity area, as expected. Secondly, the linear theory including the nonlinear leading-edge corrections appears to be much closer (than conventional linear theory) to the nonlinear solution, especially at the leading-edge region. This is consistent with the fact that linear theory with leading-edge

corrections has been shown to predict the correct effect of foil thickness on the cavity size (Kinnas 1991). However, for small foil thicknesses and high angles of attack, the difference between linear theory with leading-edge corrections and nonlinear theory becomes larger. Therefore, the application of nonlinear theory is necessary in predicting hydrofoil or propeller cavitation accurately for arbitrary thickness to chord ratios and for on- as well as off-design conditions. Thirdly, the nonlinear cavity shapes from the first and converged iterations appear to be very close to one another. This result, in addition to the success of the first iteration in predicting the correct cavity shape for the given cavitation number, leads us to believe that the error introduced by ignoring the cavity regridding is small.

3. Partially cavitating three-dimensional hydrofoil

3.1. *Formulation*

Consider a three-dimensional partially cavitating hydrofoil, shown in figure 8, subject to a uniform inflow (potential) $U_\infty(\Phi_{in})$. The perturbation potential on the cavity and wetted hydrofoil is given by the three-dimensional Green's formula:

$$2\pi\phi_p = \iint_S \left[\phi \frac{\partial}{\partial n}\frac{1}{R} - \frac{\partial \phi}{\partial n}\frac{1}{R}\right] dS + \iint_W \Delta\phi_w \frac{\partial}{\partial n}\frac{1}{R} dS \quad \text{on} \quad S. \tag{21}$$

The hydrofoil and cavity surface are discretized into N chordwise and M spanwise quadrilateral panels, in the same way as in the case of fully wetted flow (full-cosine spacing in both directions) (Lee 1987; Kerwin *et al.* 1987). A typical panel arrangement for a rectangular hydrofoil with $N = 100$ and $M = 20$ (over the half-span) will be shown in figure 10. The panels representing the cavity are located on the hydrofoil surface underneath it. We use constant-strength source and dipole panels on the foil and constant-strength dipole panels on a presumed wake surface. In the present work we assume that the wake follows the unperturbed flow. The dipole strength in the wake, $\Delta\phi_w$, is kept constant in the direction of the inflow. Its value in the spanwise direction may be variable and is set equal to the difference of potentials at the upper and lower trailing-edge panels on the same spanwise strip (Morino's condition, Morino & Kuo 1974). The kinematic boundary condition on the wetted portion of the foil defines the source strength there in terms of the known inflow velocity:

$$\frac{\partial \phi}{\partial n} = -\frac{\partial \Phi_{in}}{\partial n} = -\boldsymbol{U}_\infty \cdot \hat{\boldsymbol{n}}. \tag{22}$$

The dynamic boundary condition on the cavitating portion of the foil requires that the pressure everywhere on the cavity be constant and equal to the known cavity pressure, p_c. By applying Bernoulli's equation, the magnitude of the total velocity on the cavity, $\boldsymbol{q}_t$, is expressed as

$$q_t \equiv |\boldsymbol{q}_t| = U_\infty (1+\sigma)^{\frac{1}{2}} [1 - f(s_f)] \tag{23}$$

where σ and $f(s_f)$ are defined by (6) and (11), respectively. On the other hand, the velocity $\boldsymbol{q}_t$ can also be expressed in terms of the derivatives of the total potential $\Phi = \Phi_{in} + \phi$ with respect to the (generally non-orthogonal) curvilinear coordinates on the cavity surface† s (chordwise) and v (spanwise) as shown in figure 8:

$$\boldsymbol{q}_t = \nabla\Phi = \frac{(\partial\Phi/\partial s)[\hat{\boldsymbol{s}} - (\hat{\boldsymbol{s}}\cdot\hat{\boldsymbol{v}})\hat{\boldsymbol{v}}] + (\partial\Phi/\partial v)[\hat{\boldsymbol{v}} - (\hat{\boldsymbol{s}}\cdot\hat{\boldsymbol{v}})\hat{\boldsymbol{s}}]}{\|\hat{\boldsymbol{s}}\times\hat{\boldsymbol{v}}\|^2} + \frac{\partial\Phi}{\partial n}\hat{\boldsymbol{n}} \tag{24}$$

† The subscript c denoting the cavity surface is omitted for convenience.

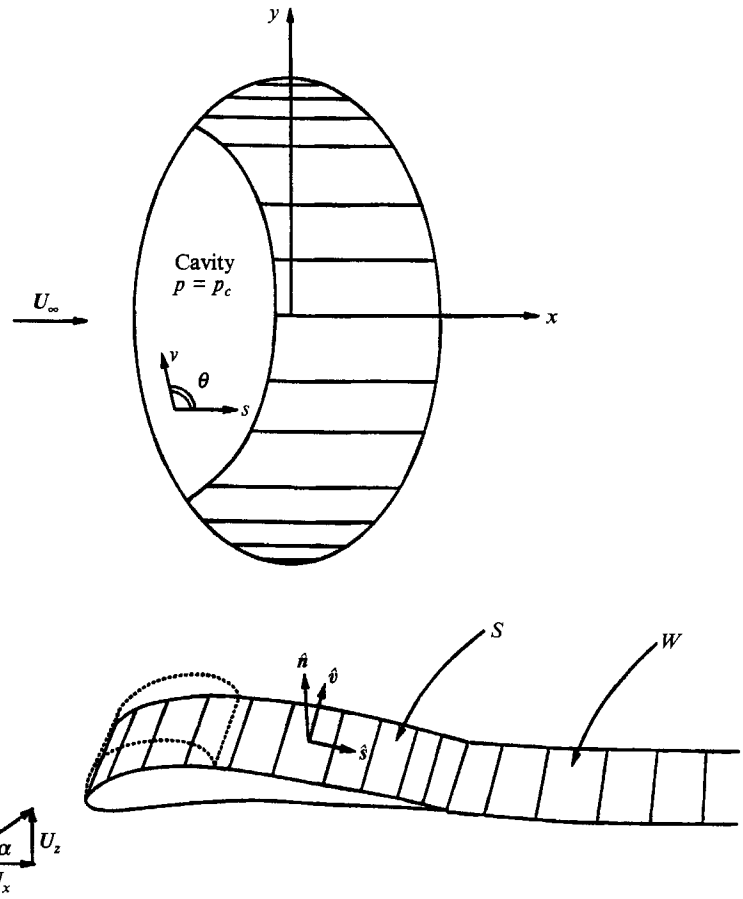

FIGURE 8. Partially cavitating three-dimensional hydrofoil. The bottom sketch shows a typical spanwise strip.

with $\hat{s}$ and $\hat{v}$ being the unit vectors corresponding to the coordinates s and v, respectively, and with $\hat{n}$ being the unit normal vector to the cavity. If s, v and n were located on the correct cavity surface, then $\partial\Phi/\partial n$ would vanish. However, this is not the case since, as mentioned at the beginning of this section, the cavity curvilinear coordinates are approximated by those on the hydrofoil surface. Equations (23) and (24) may be combined to form an equation which is quadratic in the unknown chordwise perturbation velocity, $\partial\phi/\partial s$. Solving this quadratic equation, we can express $\partial\phi/\partial s$ in terms of the cavitation number, the inflow potential, and the unknown crossflow $\partial\Phi/\partial v$:

$$\frac{\partial\phi}{\partial s} = -\frac{\partial\Phi_{in}}{\partial s} + \frac{\partial\Phi}{\partial v}\cos\theta + \sin\theta\left[q_c^2[1-f(s)]^2 - \left(\frac{\partial\Phi}{\partial v}\right)^2\right]^{\frac{1}{2}} \tag{25}$$

with θ being the angle between $\hat{s}$ and $\hat{v}$ as shown in figure 8, and $q_c = U_\infty(1+\sigma)^{\frac{1}{2}}$. Note that $(\partial\Phi/\partial n)^2$ is omitted from (25), since its value is second order in h as can be seen from (27). The correct root of the quadratic equation was determined by ensuring that the two-dimensional result, (10), may be recovered from (25).

Equation (25) is integrated once to form a Dirichlet boundary condition on ϕ:

$$\phi(s) = \phi(0) - \Phi_{in}(s) + \Phi_{in}(0) + \int_0^s \left\{\frac{\partial\Phi}{\partial v}\cos\theta + \sin\theta\left[q_c^2[1-f(s)]^2 - \left(\frac{\partial\Phi}{\partial v}\right)^2\right]^{\frac{1}{2}}\right\} \mathrm{d}s. \tag{26}$$

Equations (25) and (26) reduce to (10) and (14), respectively, in two dimensions. The integral on the right-hand side of (26) is determined by trapezoidal quadrature.

The planform of the cavity, $l(y)$, is unknown and has to be determined as a part of the solution. However, the problem of determining the cavity shape at a prescribed ('guessed') planform will be addressed first. The location of the cavity detachment point, $l_D(y)$ is an input parameter and is kept fixed throughout the solution. The effect of the location of the cavity detachment on the solution as well as a discussion on how to determine it, are given in §5. For a given cavity planform, $l(y)$, the discretized version of (21) is applied at the control points of all $N\times M-N_{sp}$ panels. N is the number of panels distributed around the chord of the foil, M is the number of panels distributed spanwise, and N_{sp} is the number of panels which are 'split' by the trailing edge of the cavity (the panels are not adapted to the cavity boundary). To avoid ambiguity, in the case where the cavity trailing edge cuts more than one panel on the same spanwise strip, the split panel is defined as the one for which the segment connecting the midpoints of its sides along the span is intersected by the trailing edge of the cavity. The $N\times M-N_{sp}$ unknowns are the dipole strengths (potentials) at the wetted panels and the source strengths at the cavity panels. The cavitation number, σ, is known and equal to its prescribed value. The potentials on the cavity panels are given by (26) and the source strengths of the wetted panels are given by (22). The value of $\phi(0)$ in (26) is also an unknown and is expressed via a cubic extrapolation in terms of the unknown potentials on the wetted panels on the same strip in front of the cavity. The source and dipole strengths on the split panels are defined as averages, as they were in two dimensions (see (20)), with the weights l_L and l_R taken as the lengths at the midspan of the split panels. The value of the spanwise velocity $\partial\Phi/\partial v$ on the right-hand side of (26) is unknown and is determined iteratively. Its initial value is set equal to the fully wetted crossflow and its subsequent values are determined from differentiation of the potentials from the previous iteration. The convergence of the crossflow term has been found to be virtually immediate, requiring at most one additional iteration. Once the problem has been solved for a guessed cavity planform, and $\partial\phi/\partial n$ at the cavity panels is known, the cavity height, $h(s,v)$, can be determined by integrating the following partial differential equation:

$$\frac{\partial h}{\partial s}\left[\frac{\partial\Phi}{\partial s}-\cos\theta\frac{\partial\Phi}{\partial v}\right]+\frac{\partial h}{\partial v}\left[\frac{\partial\Phi}{\partial v}-\cos\theta\frac{\partial\Phi}{\partial s}\right]=\sin^2\theta\left[\frac{\partial\phi}{\partial n}+\frac{\partial\Phi_{in}}{\partial n}\right]. \tag{27}$$

Equation (27) results from the condition $\nabla\Phi\cdot\hat{\boldsymbol{n}}_c=0$ on the cavity, with $\nabla\Phi$ given by (24) and with $\hat{\boldsymbol{n}}_c$ being the normal to the cavity surface. It can be proven that, to first order in h, $\hat{n}_c$ can be expressed as

$$\hat{\boldsymbol{n}}_c=\frac{-(\partial h/\partial s)[\hat{\boldsymbol{s}}-(\hat{\boldsymbol{s}}\cdot\hat{\boldsymbol{v}})\,\hat{\boldsymbol{v}}]-(\partial h/\partial v)[\hat{\boldsymbol{v}}-(\hat{\boldsymbol{s}}\cdot\hat{\boldsymbol{v}})\,\hat{\boldsymbol{s}}]}{\|\hat{\boldsymbol{s}}\times\hat{\boldsymbol{v}}\|^2}+\hat{\boldsymbol{n}}, \tag{28}$$

where $\hat{s}$, $\hat{v}$ and $\hat{\boldsymbol{n}}$ correspond to the curvilinear coordinates of the hydrofoil surface under the cavity. The partial differential equation (27) reduces to the ordinary differential equation (16) in two dimensions. The partial differential equation is solved recursively by replacing the chordwise derivative, $(\partial h/\partial s)$, and the spanwise derivative, $(\partial h/\partial v)$, with two-point backwards-difference formulae. The height of the cavity at its trailing edge, $\delta(y)$, will not be zero in general, unless we have guessed the correct cavity planform.

The described method is applied to a rectangular hydrofoil with a NACA65a cross-section which is 5% thick at the midspan, tapering elliptically to zero thickness at the

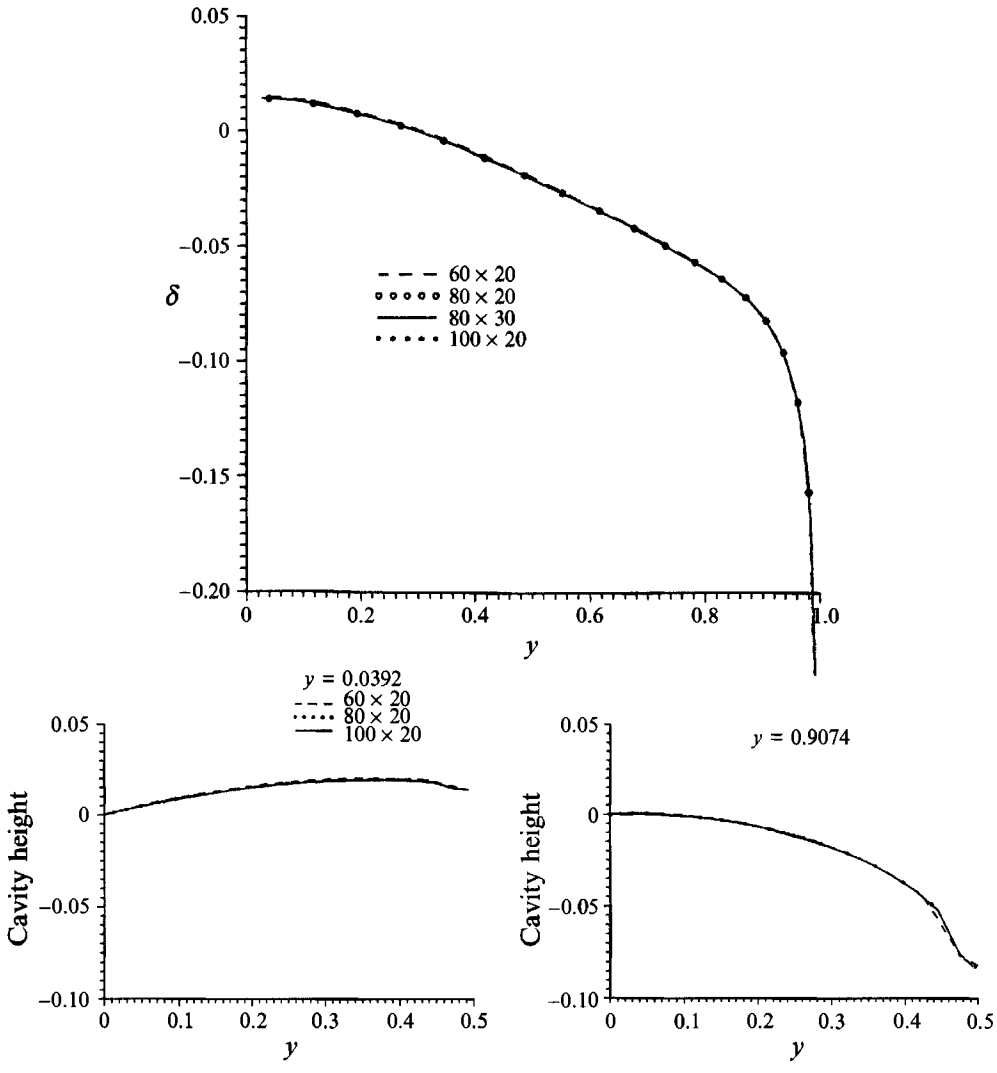

FIGURE 9. Spanwise and chordwise cavity thickness distributions predicted from the present BEM and for varying $N \times M$. Rectangular hydrofoil with a NACA65a cross-section with $t/c = 0.05$ at midspan, tapering elliptically to zero thickness at the tip, $\alpha = 4°$, $\sigma = 0.4$. The twist angle, in degrees, is given by $\alpha_t(y) = 8y^3 - 12y^2$ (midspan at $y = 0$, tip at $y = 1$). The cavity planform is rectangular with $l_D(y) = 0.024$ and $l(y) = 0.5$.

tip, and an angle of attack of 4°. Note that in all ensuing figures, x will be normalized on the local chord length, and y will be normalized on the half-span. (In the test cases the hydrofoil is taken to be symmetric about $y = 0$, and thus only the flow about the half-span need be computed.) The cavity planform is also rectangular with $l_D(y) = 0.024$ and $l(y) = 0.5$. The convergence of the predicted spanwise and chordwise cavity thickness distributions with number of panels is shown in figure 9. Perspectively plots of the cavity shapes corresponding to two other cavity planforms are shown in figure 10. Figure 10 suggests that the three-dimensional behaviour appears to be an extension of the two-dimensional behaviour in that a cavity which is too short at a given radius has a locally positive δ, while one which is too long has a locally negative δ. Figure 10

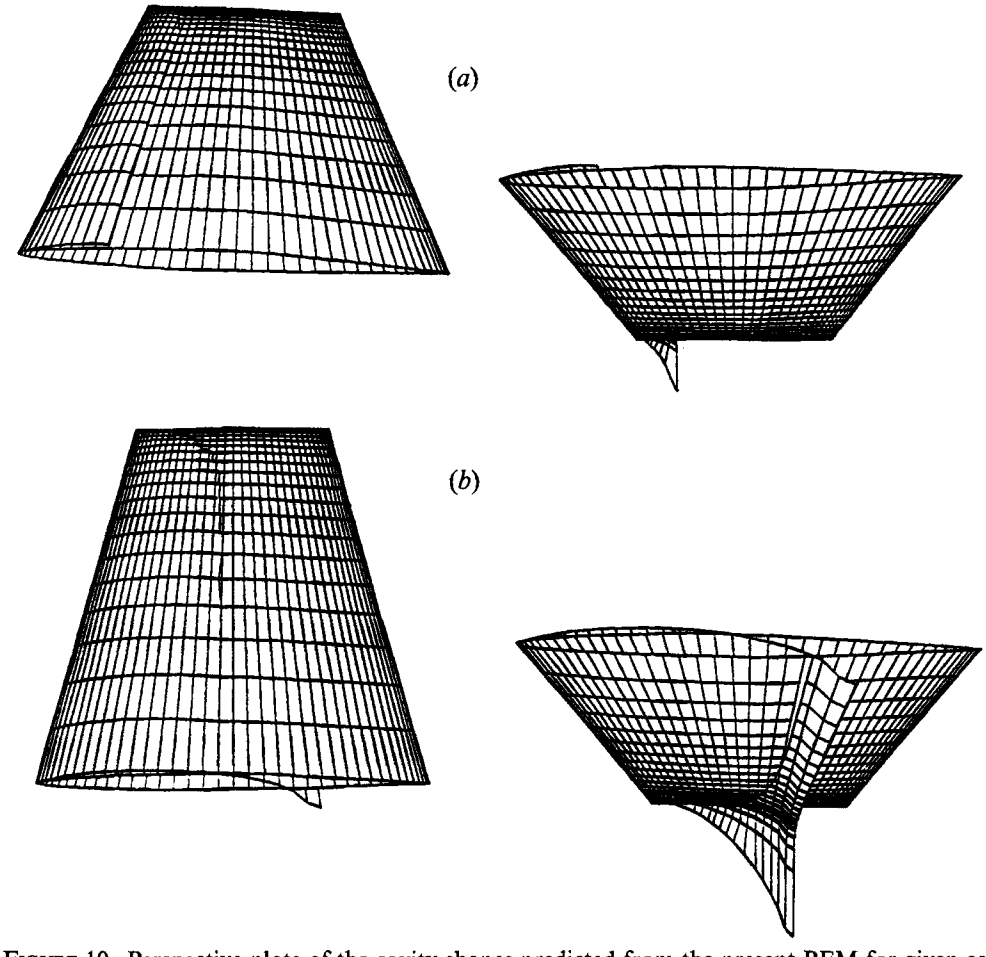

FIGURE 10. Perspective plots of the cavity shapes predicted from the present BEM for given cavity planforms. Same rectangular hydrofoil and flow conditions as in figure 9. Rectangular cavity planform with (*a*) $l(y) = 0.2$ and (*b*) $l(y) = 0.7$. In both cases $\sigma = 0.4$ and $l_D(y) = 0$ for all y. The cavity shapes are generated by drawing the predicted cavity thickness normal to the foil surface. Negative cavity thicknesses indicate that the given cavity planforms are not 'correct'.

also suggests that the correct cavity planform for this example is roughly parabolic and probably zero near the tip of the foil and maximum at the midspan. A procedure for determining the correct cavity planform will be described in the next subsection.

3.2. *An algorithm for determining the three-dimensional cavity planform*

In a similar manner as in two dimensions we find the correct (discretized) cavity planform by solving, with respect to the M unknowns, $l_1, l_2, \ldots, l_M$, the system of equations

$$\delta_m(l_1, l_2, \ldots, l_M; \sigma) = 0, \quad m = 1, \ldots, M, \tag{29}$$

where δ_m is the openness of the cavity trailing edge at the mth spanwise strip and l_m is the cavity length at midspan of the same strip. The system of equations (29) is solved iteratively by applying an M-dimensional Newton–Raphson (secant method) scheme. The updated cavity lengths for the $(k+1)$th iteration are given as follows:

$$\boldsymbol{L}^{k+1} = -\boldsymbol{J}^{-1}\boldsymbol{\delta}^k + \boldsymbol{L}^k \tag{30}$$

where $$L^{\mathrm{T}} = [l_1\, l_2\, l_3 \ldots l_m], \quad \delta^{\mathrm{T}} = [\delta_1\, \delta_2\, \delta_3 \ldots \delta_m],$$

and where $\boldsymbol{J}$ is the Jabobian, which has elements

$$J_{ij} = \frac{\partial \delta_i}{\partial l_j}, \quad 1 \leqslant i,j \leqslant M.$$

Ideally, we would like to approximate each element of the Jacobian by using a two-point finite-difference scheme (often called the secant method). This would mean that the system of equations given by (20), (21), and (25) would have to be solved $M+1$ times for each Newton–Raphson iteration. Even in the case of an accurate initial guess, this scheme clearly would be prohibitively expensive. Fortunately, the iterative method may be accelerated by applying a locally scalar Newton–Raphson (secant method) scheme at each spanwise strip, which is equivalent to ignoring the off-diagonal terms of the Jacobian in solving (30) for the updated cavity planform. The second guess of the planform in the secant method is taken to be a perturbation of the initial guess by a fixed amount (4.0 % of the local chord length c_m) in the direction determined by the sign (in an average sense) of $\delta(y)$ which resulted from the initial guess. In general, this method will not be stable, due to the importance of the off-diagonal terms of the Jacobian, which have been ignored. However, numerical damping has been found to render the method stable by prohibiting each cavity length l_m from changing by an amount greater than a multiple of the local δ_m, $|\Delta l_m| = |k * \delta_m|$. In the event that $|\delta_m|$ is large, the change in length is bounded by $|\Delta l_m| \leqslant 0.05 c_m$. The convergence history has been found to be weakly dependent on k, and $k = 10$ yields satisfactory convergence. Equation (29) is satisfied within a desired tolerance for the maximum value of $|\delta_m|$, which we have taken equal to 8×10^{-4}.

Originally, the cavity trailing edge was adjusted at each spanwise location to match the panel boundaries closest to it. In that case, the objective was to 'trap' the zero-thickness trailing-edge cavity inside one panel at each spanwise location and then to interpolate the solutions corresponding to the 'left' and 'right' boundaries of the panel. However, this algorithm for determining the cavity planform was found to be very unstable and to converge to different planforms with increasing number of panels. The failure of the scheme was attributed to the discretization of the cavity trailing edge which in some cases resulted in highly discontinuous cavity planforms in the spanwise direction. In order to produce smoother discretizations of the cavity planform in the spanwise direction, the split-panel technique, described already, was devised. This technique also allowed for a continuous spectrum of cavity lengths in the chordwise direction. The split-panel technique has been found to substantially improve the convergence of the method to the correct cavity planform.

To supply the reader with some understanding of the three-dimensional behaviour of the cavity openness in the vicinity of the correct cavity planform, determined by applying the described method, figure 11 shows the spanwise distribution $\delta(y)$ for various cavity planforms on a rectangular hydrofoil. Among these cavity planforms, some lie to the left of the zero-δ planform (curve 5 in the figure) and some lie to the right. Notice that $\delta(y)$ corresponding to each planform that lies to the left of the correct planform is everywhere positive while for those corresponding to the planforms to the right of the correct one, $\delta(y)$ is everywhere negative. Figure 11 can be viewed as the analogue of figure 4 in three dimensions.

When searching for the correct cavity length on two-dimensional hydrofoils, (19) was solved subject to the condition $\mathrm{d}\delta/\mathrm{d}l < 0$, in order to exclude 'long' unstable partial cavities. However, it was not necessary to impose a similar condition when

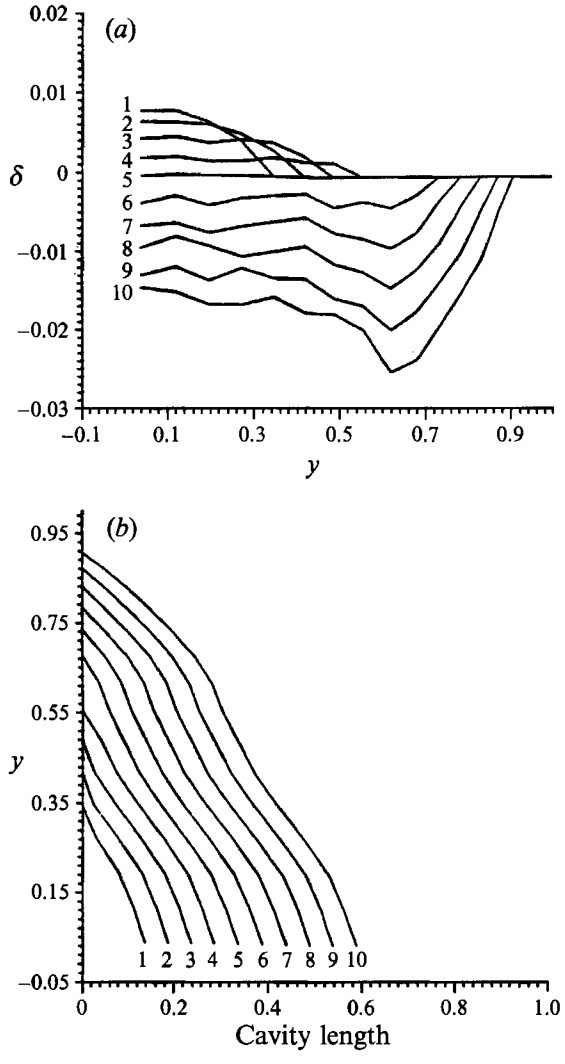

FIGURE 11. (*a*) Spanwise cavity openness distributions, $\delta(y)$, for the various cavity planforms shown in (*b*). Same rectangular hydrofoil and flow conditions as in figure 9. In all cases $\sigma = 0.4$. Each $\delta(y)$ distribution corresponds to the planform with the same number.

searching for the correct cavity planform on three-dimensional hydrofoils. In figure 12, the cavity planforms predicted by the present method at different cavitation numbers are shown for the elliptic hydrofoil (whose complete geometry is described in the next section) of maximum thickness to chord ratio equal to 0.06 at all spanwise locations. Notice that as the cavitation number decreases, the predicted cavity planform becomes longer at all spanwise locations until the cavity approaches the trailing edge at the midspan of the foil. This behaviour appears to be different from the two-dimensional one where the minimum value of cavitation number occurs before the cavity reaches the trailing edge, at around 75% of the chord. For all cavity planforms shown in figure 12, as well as those shown in the rest of the paper, it has been found that the slopes $\partial\delta_m/\partial l_m$ at all spanwise locations of the converged solution were negative, even though this was not required in the solution. The above observations indicate that there is only one partially cavitating solution for the three-dimensional hydrofoil geometries which

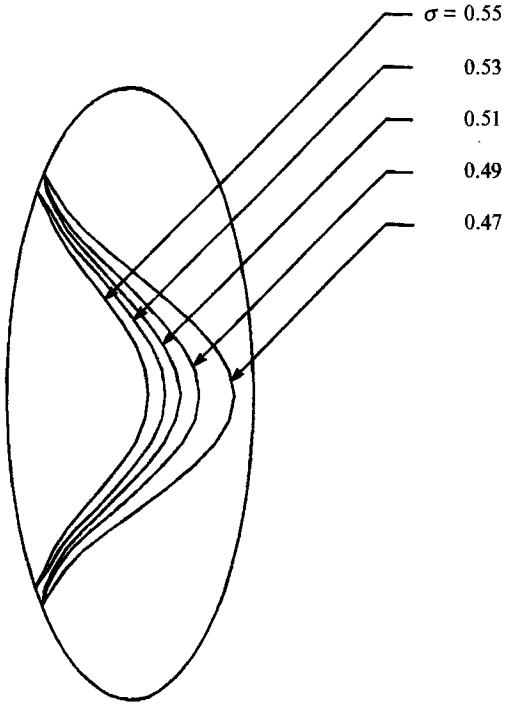

FIGURE 12. Predicted cavity planforms at various cavitation numbers on an elliptic hydrofoil with $t/c = 0.06$, at $\alpha = 4°$. The twist angle, in degrees, is given by $\alpha_t(y) = 8y^3 - 12y^2$ (midspan at $y = 0$, tip at $y = 1$).

were investigated. However, there may be solutions (for example with sharp changes of the cavity length in the spanwise direction) which we have missed. The subject of multiple solutions will not be addressed, beyond conjecture, in this work.

To summarize, in the present algorithm we start from an initial guess and adjust the cavity planform globally until the thickness at its trailing edge becomes equal to zero. At each trial cavity planform, the nonlinear (first iteration) three-dimensional cavity solution is achieved with the cavitation number being known. In contrast, in the algorithm developed by Jiang & Leehey (1977) and Lee (1979), the cavity planform is adjusted locally at each spanwise location (with the effect of the other strips accounted for in an iterative sense) until the computed cavitation number becomes equal to the desired one. At each trial cavity length, the linearized cavity solution with zero cavity thickness at the trailing edge is obtained and the corresponding unknown cavitation number is determined.

3.3. *Results and numerical validation*

In this section, results are discussed for a rectangular hydrofoil and two elliptic hydrofoils at various angles of attack and various cavitation numbers. All foils that we considered have a maximum chord to span ratio equal to 0.17. In each example, the foil is twisted in the spanwise direction such that the angle of attack is zero at the tip (this is true also in figures 9–12). This is done to ensure that there is no tendency to supercavitate at the tip, since the subject of supercavitation has not been addressed in this work. The amount of twist at different spanwise locations y ($0 < y < 1$) is taken equal to $-\alpha(3y^2 - 2y^3)$, with α being the angle of attack (twist is positive in the direction of positive α).

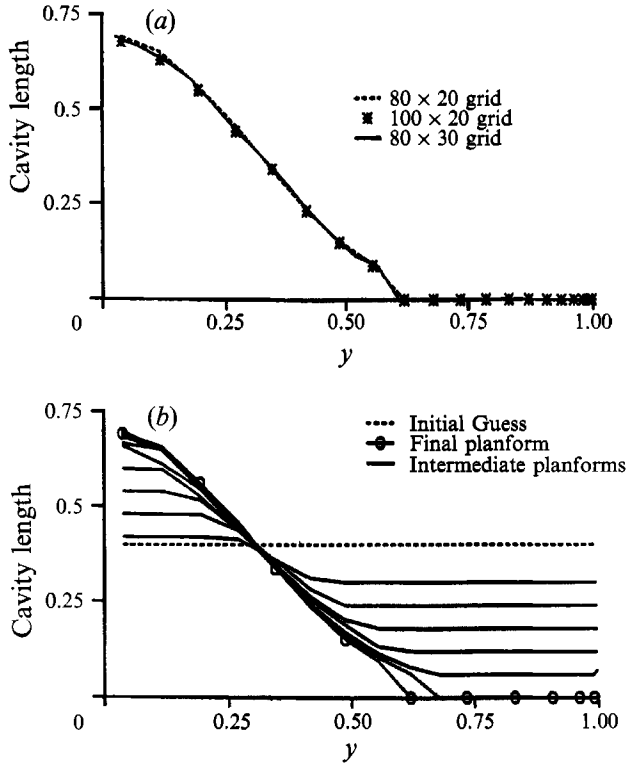

FIGURE 13. (*a*) Convergence of cavity planform with numbers of chordwise and spanwise panels. (*b*) The convergence history for the 100 × 20 grid. Same rectangular hydrofoil and flow conditions as in figure 9.

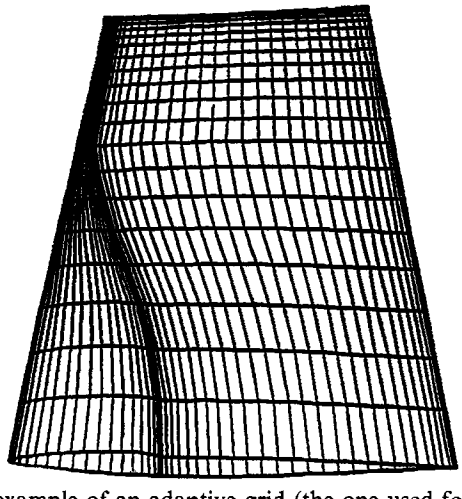

FIGURE 14. An example of an adaptive grid (the one used for validation of the cavity solution in figure 15).

Figure 13(*a*) shows the converged cavity planform on a rectangular hydrofoil for various panel arrangements. The initial guess in each case was a uniform cavity length ($l(y) = 0.4$ for all y). In an effort to show that the solution converges, the number of panels has been varied from 1600 (80 chordwise, 20 spanwise), to 2400 (80 × 30). Figure

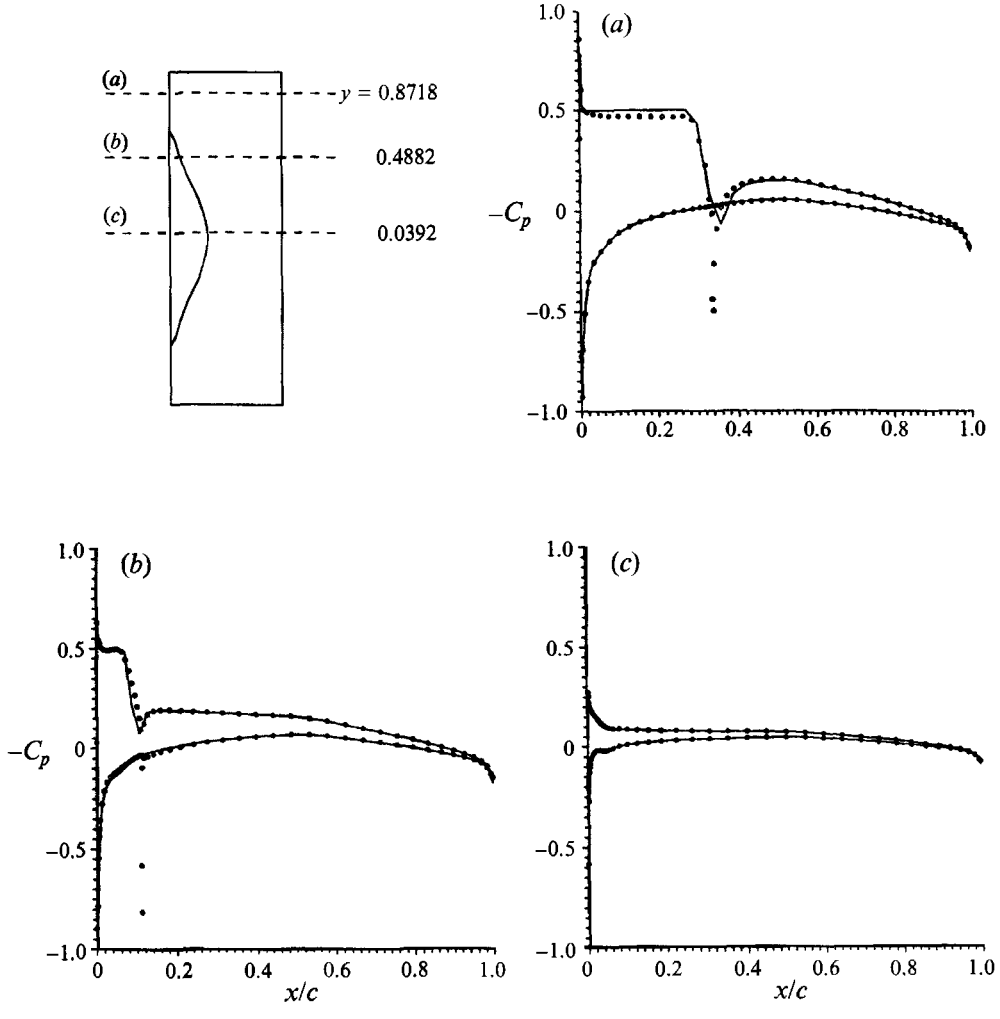

FIGURE 15. Validation of the cavity solution. Pressure distributions shown at various spanwise locations: (*a*) $y = 0.0392$, (*b*) $y = 0.4882$, (*c*) $y = 0.8718$. Same rectangular hydrofoil as in figure 9, $\alpha = 3°$, $\alpha/\sigma = 0.105$, $l_D(y) = 0.004$. · · · ·, Fully wetted solution; ——, cavity solution.

13(*b*) shows the sequence of cavity planforms in the convergence history for the 100×20 grid.

To validate the solution, a new three-dimensional hydrofoil geometry is created by combining the computed cavity and foil to form a single surface, where the grid on the new foil has been adapted to conform to the cavity planform and shape, (as for example is shown in figure 14). In other words, the panels representing the cavity are placed on the predicted cavity surface. The flow around the new foil is then analysed with an independent fully wetted analysis method (Kerwin *et al.* 1987) and the resulting pressure distribution is compared to the pressure from the cavity solution. The pressures from the cavity solution are computed by differentiating the potentials from the cavity solution on the surface of the foil to find velocities and then by applying Bernoulli's equation. If the cavity shape is the correct one which corresponds to the applied dynamic boundary condition, then the two pressure distributions will match. The discrepancy between the two pressure distributions is therefore a measure of the

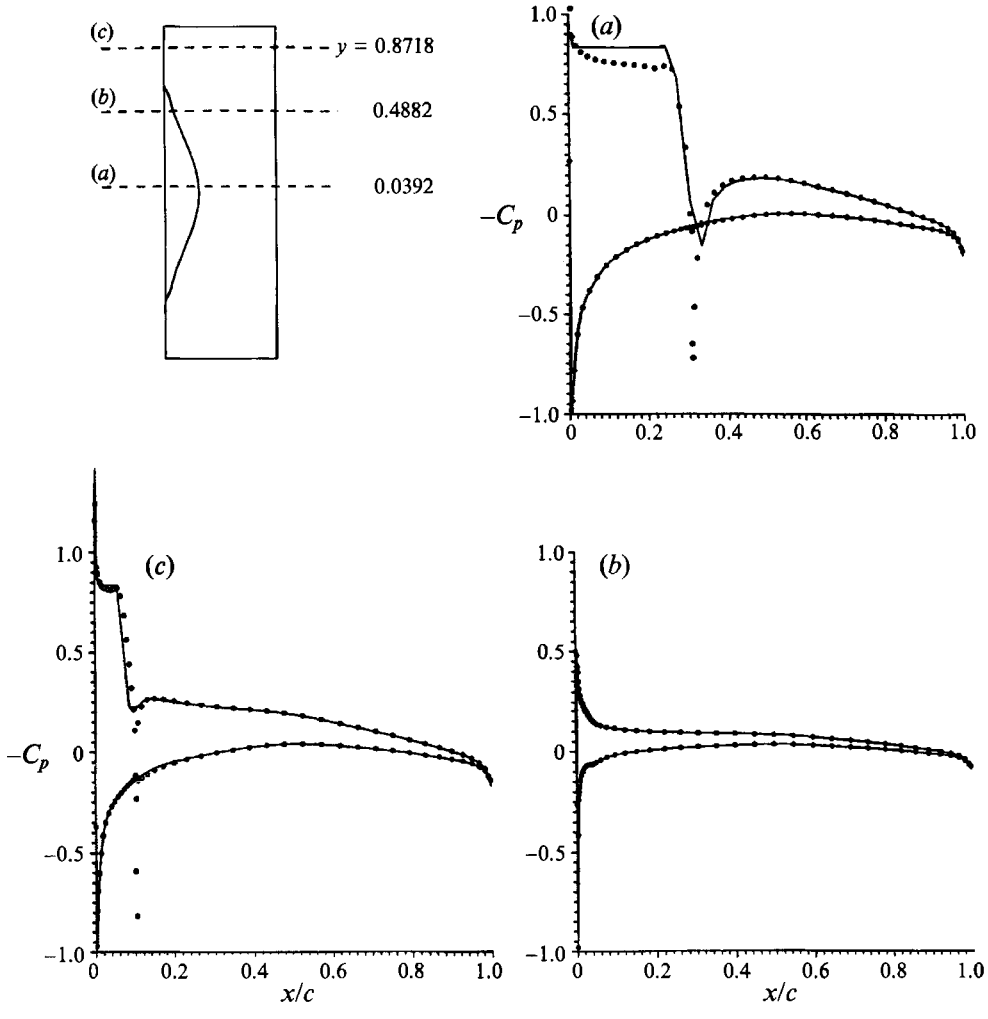

FIGURE 16. Same as figure 15 but for $\alpha = 5°$.

accuracy of the cavity solution presented. We refer to the comparison of the two pressure distributions as the 'pressure validation test'. Figures 15 and 16 show this comparison, which in general is very good. Notice that the pressure distribution from the cavity solution is constant everywhere on the cavity, as required by the dynamic boundary condition (based on the same formulation as the pressure calculation). In addition, notice that the comparison between the two pressure distributions deteriorates with increasing angle of attack. This indicates that the shape of the cavity from the first iteration is further from the correct nonlinear shape for higher angles of attack. More importantly, however, the results for two-dimensional hydrofoils, discussed in §2, have shown that the difference between the first iteration and converged cavity lengths and volumes is not substantial, even at moderately high angles of attack (see figure 7). In other words, from our experience in applying the same validation test in two dimensions, the pressure distributions from the first and the converged nonlinear solutions have a larger error than the corresponding cavity extents and shapes (see for example figure 6).

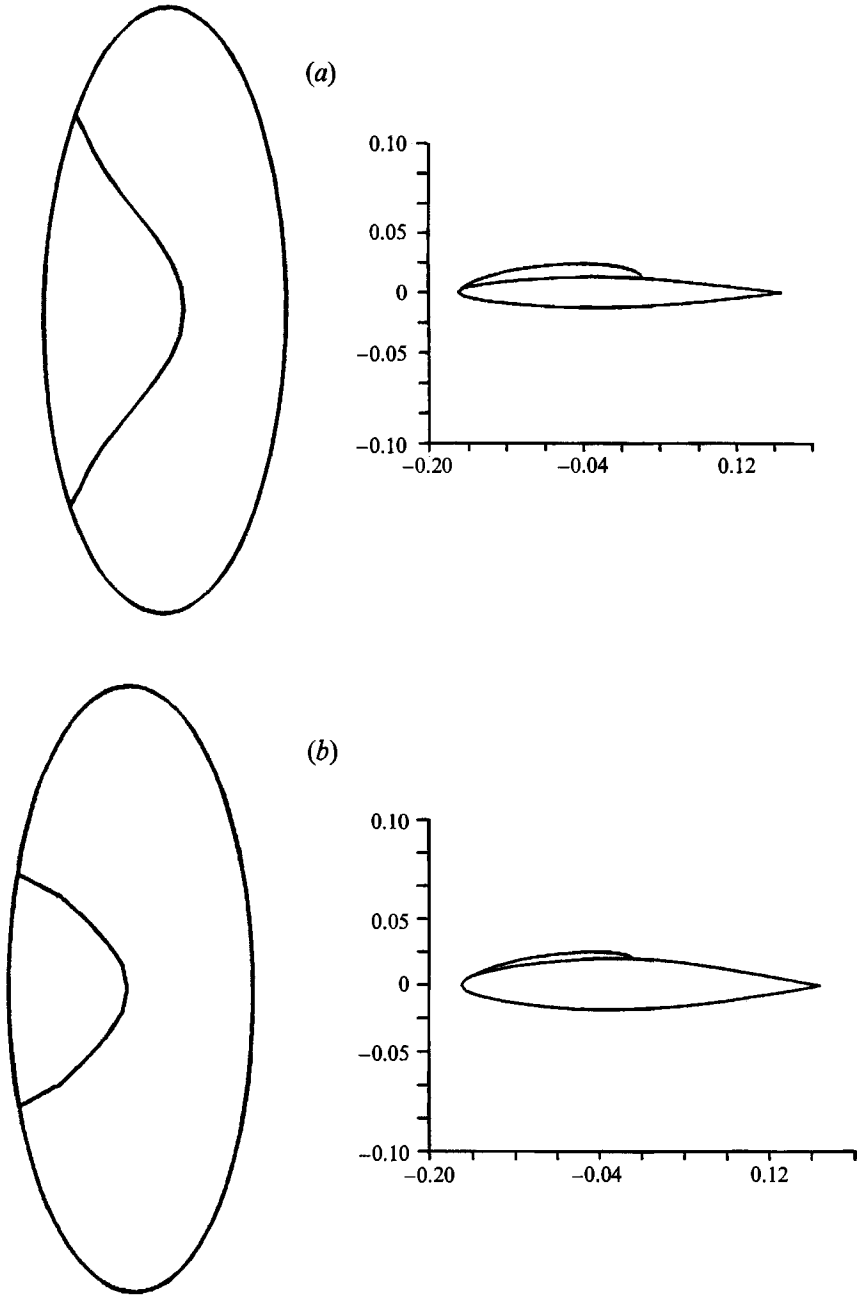

FIGURE 17. Expanded cavity planform for an elliptic hydrofoil with (*a*) $t/c = 6\%$ and (*b*) $t/c = 9\%$, at $\alpha = 4°$, $l_D(y) = 0$, $\sigma = 0.55$. Also shown are cross-sections of the foil and cavity at midspan.

Also noteworthy in figures 15 and 16 is the fact that the pressures near the tip, away from the cavitating portion of the foil, are higher than the cavity pressure (this is also true for the other non-cavitating tip sections which are not shown in the figures). If this were not the case, the converged cavity planform would not be correct.

The sample runs and validation tests for this work were done on an IRIS 4D/25 TG.

As an example, the CPU time required to produce one of the perspective plots in figure 10, which used a 100×20 grid, was 40 minutes.

Finally, results for the two elliptic three-dimensional hydrofoils are shown in figure 17. Both hydrofoils have the same planform and the appropriate twist as discussed in the beginning of this subsection. They have a NACA65a thickness distribution in the chordwise direction with a constant maximum thickness to chord ratio in the spanwise direction. The maximum thickness to chord ratio for these hydrofoils is 0.06 and 0.09, respectively. They are both subject to a uniform inflow at an angle of attack $\alpha = 4°$ and at a cavitation number $\sigma = 0.55$. Figures 17 and 18 show that the predicted cavity extent (in both chordwise and spanwise directions) and volume decrease with increasing thickness. A similar nonlinear effect of foil thickness on the cavity shape has already been shown in two dimensions by many researchers (Tulin & Hsu 1980; Uhlman 1987; Kinnas 1991). The pressure validation test was also done for the elliptic hydrofoil, and the pressures at the fully wetted tip were checked to confirm that the cavity planforms are acceptable.

4. Comparison to experimental measurements

In order to validate the present method, a systematic comparison to experimental results is desirable. Since the main contribution of this work is the accurate prediction of partial cavity planforms on three-dimensional hydrofoils, comparison to measurements in steady three-dimensional flow is preferable. Unfortunately, we were unable to find published experimental measurements of steady flow, partially cavitating, three-dimensional hydrofoils in the literature. In order to fill the void, we decided to perform a simple experiment in the MIT Marine Hydrodynamics Lab Variable Pressure Water Tunnel. Lack of tunnel time, as well as lack of funds for design and manufacture of equipment, drove us to use an existing wing and fairing configuration.† The goal of the experiment was to measure the cavity planform in steady uniform flow at reduced ambient pressure and to make comparisons to the results of the present method. The experimental cavitation number was obtained by measuring the streamwise velocity component, using a laser-Doppler velocimeter, at points along a line approximately normal to the cavity surface, including a point on or very near to the cavity surface. This was done at a location near the wing root where the spanwise flow on the cavity surface was expected to be negligible and at a chordwise position where the (unperturbed) streamwise direction was nearly tangent to the cavity. At this location, the measured velocity provides a very good estimate for the cavity velocity q_c. The cavitation number is then computed from the well-known expression $\sigma = 1 - q_c^2$. This method of determining σ had previously been applied by Kinnas & Mazel (1992) to compare numerical results and experimental measurements of the flow around two-dimensional supercavitating hydrofoils. Its origin was influenced by the inability to obtain an accurate estimate of the cavity pressure (used in the definition of σ), in part because the vapour pressure varies strongly with temperature and, in addition, because of the unknown air content inside the cavity. The experiment was performed for the wing described by figure 18 and table 1. The wing, a windsurfer fin made by FINTECH, was mounted vertically in the tunnel, attached to a finbox which in turn was attached to the dynamometer shaft. While forces were not measured in this experiment, the dynamometer setup was convenient for our configuration. The finbox is an aluminium rectangular box serving as a housing for the standard Tuttle box which

† Courtesy of Professor Sheila Widnall of MIT Department of Aeronautics and Astronautics and Graduate Student William Gorgen.

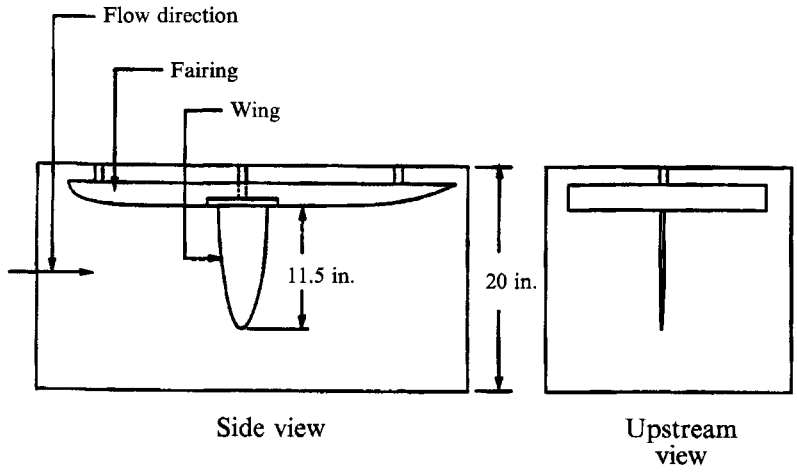

FIGURE 18. Experimental configuration.

y/R	X_{LE}/R	X_{TE}/R	c/D	t_{max}/D	rake/D
0	—	—	0.1902	0.0213	0
0.0757	0.2197	−0.1527	0.1862	0.0211	0
0.1270	0.2150	−0.1526	0.1840	0.0210	0.0012
0.2297	0.2033	−0.1558	0.1795	0.0206	0.0049
0.3324	0.1914	−0.1558	0.1736	0.0199	0.0079
0.4351	0.1772	−0.1537	0.1654	0.0188	0.0109
0.5378	0.1606	−0.1477	0.1540	0.0170	0.0135
0.6405	0.1420	−0.1371	0.1395	0.0148	0.0156
0.7432	0.1194	−0.1213	0.1203	0.0126	0.0175
0.8459	0.0916	−0.0976	0.0945	0.0096	0.0183
0.8973	0.0743	−0.0801	0.0772	0.0067	0.0182
0.9486	0.0519	−0.0566	0.0542	0.0030	0.0179
1.0000	—	—	0	0	0.0179

TABLE 1. Geometry of the experimental wing: X_{LE} and X_{TE} are the measured x-components of the leading edge and trailing edges of the wing, respectively, from which the other quantities were deduced. $R = \frac{1}{2}D$; R is the half-span of the wing and t its thickness.

typically connects the fin to the board. Since the finbox is a bluff body with sharp corners, it was necessary to use a fairwater to streamline the flow. The angle of attack of the wing was $\alpha = 6.5°$ and the flow speed was $U_\infty = 6.83$ m/s. Measurements were made for two cavitation numbers, $\sigma_1 = 1.084$ and $\sigma_2 = 1.148$, corresponding to ambient pressures of 320 and 370 mmHg, respectively. The position of the cavity detachment and reattachment points were measured at six spanwise locations, using the laser and its motion/location instrumentation.

The computations were performed for the measured cavitation numbers, using the measured detachment points as input. The detachment points were taken at $l_D(y)/c(y) = 0.024$, with $c(y)$ being the local chord, for both cavitation numbers. The computations assume that the wing is attached to an infinite flat plate, in place of the fairwater, allowing the reflection of the wing across the plate to account for the presence of the wall. A comparison of the measured and predicted cavity planforms is shown in figure 19. One important characteristic of the solution near the tip should be

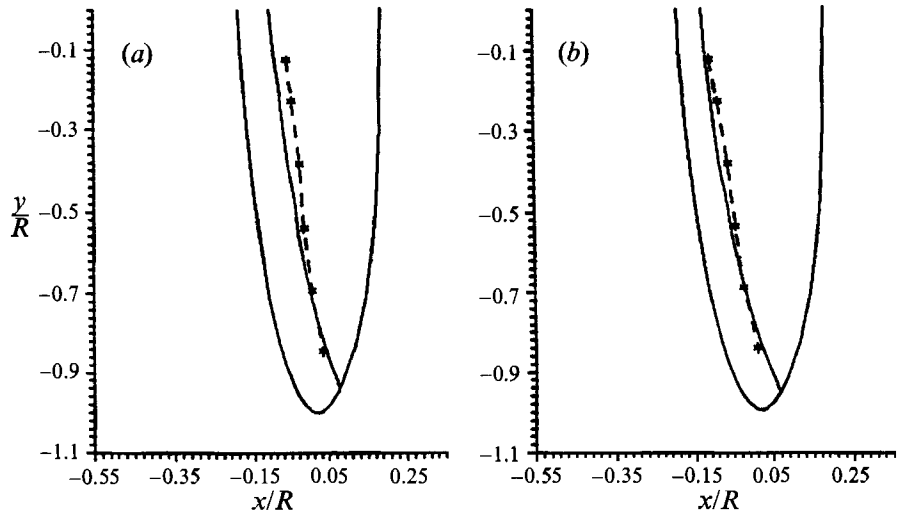

FIGURE 19. Measured (-*-*-*-) and predicted (——) cavity planforms. (*a*) $\sigma_1 = 1.084$, (*b*) $\sigma_2 = 1.148$.

mentioned here: the method is not able to find a closed partial cavity in the tip region, which indicates that the solution at the tip should be a supercavity matched to a local tip solution to capture the effect of the cavitating tip vortex. The presence of the tip vortex was also detected in the experiment.

The comparison shown in figure 19 shows good agreement between the prediction of the present method and the experimental measurements. However, several cautionary comments should be made. First, owing to a difficulty in the measurement of the angle of attack, α is accurate only to $\pm 0.5°$. Second, the analysis does not include the effect of the tunnel sidewalls, nor that of the tunnel floor. However, owing to the relatively small dimensions of the wing and its cavity, the wall effects are expected to be small. Next, the cross-section of the wing was assumed to be a member of the NACA65a series (Abbott & Von Doenhoff 1959) with the measured maximum thicknesses. Although this section is believed to be close to the actual cross-section, the wing was hand-shaped and the exact cross-section is not necessarily identical to the one used in the computations. Only the maximum chordwise thickness was measured; no attempt was made to measure the thicknesses throughout the chord. The chordwise position of the maximum thickness was measured to be close to 40 % of the local chord length throughout the span. The fact that this is true also of the NACA65a section led to its selection. Finally, this experiment was not complete. A more systematic experiment would measure planforms for a greater number of cavitation numbers and angles of attack. Time limitations prevented extensive data taking for the current work.

In the light of these comments and observations, we emphasize here the qualitative agreement between theory and experiment. The good agreement evident in figure 19, while promising, is not sufficient validation of the method. Further experimental work is planned for the future.

5. Conclusions and future work

In this work, a general boundary-element method was presented for determining the cavity shape for two- and three-dimensional partially cavitating hydrofoils of arbitrary geometry. The two-dimensional analysis was done in the framework of the two

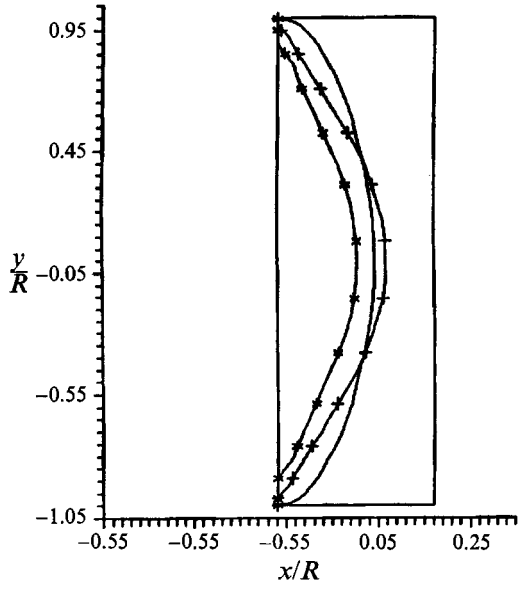

FIGURE 20. Sensitivity of predicted cavity planform to the location of the detachment line, $l_D(y)$. Planar rectangular wing, aspect ratio = 5.9, NACA65a cross-section, 9% thick at midspan, tapering elliptically to zero at the tips, $\sigma = 0.5$, $\alpha = 3°$, $N = 80$, $M = 20$. ——, $l_D(y) = 0$; ++++, $l_D(y) = 0.014$; –*–*–*–, $l_D(y) = 0.024$.

relevant boundary-value problems: one in which the cavity length is specified, and the other in which the cavitation number is known. The results of our two-dimensional study, which were summarized in §2.3.2, suggest that a remarkably accurate estimate of the fully nonlinear cavity solution may be determined without regridding, which could be prohibitively expensive in solving the three-dimensional problem. A robust and efficient method for finding the three-dimensional cavity planform and shape has been developed for the case where the cavitation number is known. In so doing, the fully three-dimensional behaviour is captured, including the nonlinear effect of foil thickness on cavity size.

The ability of the present method to treat an arbitrary cavity planform on a fixed panel discretization, makes it very suitable for the prediction of the unsteady three-dimensional hydrofoil or propeller sheet cavitation. Indeed, the method has already been extended by the authors to predict the flow around supercavitating and mixed partial/supercavitating hydrofoils (Fine & Kinnas 1992) and finally, to predict the unsteady cavitating flow around marine propellers in non-uniform inflows (Kinnas & Fine 1992; Fine 1992). However, for the method to be complete, it must ultimately account for the effects of viscosity. Arguably, the two regions where viscosity plays the most influential role are in the vicinity of the cavity detachment close to the blade leading edge, and in the cavity wake. In the future, a boundary-layer analysis will be incorporated to determine the correct detachment point, which experiments have shown to be closely correlated to the viscous flow in front of the cavity (Arakeri 1975; Franc & Michel 1985). These and other experiments have also shown that the pressures on the wetted foil in front of the cavity may be smaller than the pressure inside the cavity. The sensitivity of the solution to the location of the cavity detachment point can be seen in figure 20. It is apparent from this figure that the predicted cavity planform is affected substantially by the location of the detachment point. It should be noted that

the cavity planform with $l_D(y) = 0$ predicts negative cavity thicknesses up to approximately 3% of the chord at the leading edge for a large part of the midspan region. It is thus rejected as a non-physical solution. The other two cavity planforms, also shown in figure 20, predict cavities with positive thickness everywhere. Their viability as physical solutions though, will depend on the viscous flow analysis in front of the detachment point as mentioned earlier. The physical solution will not necessarily correspond to a uniform $l_D(y)$ across the span. To account for the viscous wake of the cavity, in the context of potential flow, an open cavity termination model may be utilized, followed by a wake with thickness equal to the displacement thickness of the corresponding boundary layer (Fabula 1962). The boundary-layer profile behind a partial cavity has been measured in experiments (Fine 1988) and its displacement thickness has been found to be appreciably larger than that of the boundary layer in fully wetted flows at the same location on the foil. Incorporating an open cavity model in our method appears to be trivial (at least in the first iteration nonlinear solution), and can be accomplished by changing the right-hand side of (29) from zero to the desired distribution of openness in the spanwise direction. In addition, the chordwise variation of the boundary layer in the wake of the cavity may be determined by coupling the present method with a boundary-layer solver.

Support of this research has been provided by the Applied Hydromechanics Research Program administered by the Office of Naval Research (Contract: N00014-90-J-1086).

REFERENCES

ABBOTT, I. H. & VON DOENHOFF, A. E. 1959 *Theory of Wing Sections*. Dover.

ACOSTA, A. J. 1955 A note on partial cavitation of flat plate hydrofoils. *Tech. Rep.* E-19.9, California Institute of Technology, Hydrodynamics Lab.

ARAKERI, H. 1975 Viscous effects on the position of cavitation separation from smooth bodies. *J. Fluid Mech.* **68**, 779–799.

BIRKHOFF, G. & ZARANTONELLO, E. H. 1957 *Jets, Wakes and Cavities*. Academic.

BRENNEN, C. 1969 A numerical solution of axisymmetric cavity flows. *J. Fluid Mech.* **37**, 671–688.

BRESLIN, J. P., VAN HOUTEN, R. J., KERWIN, J. E. & JOHNSSON, C.-A. 1982 Theoretical and experimental propeller-induced hull pressures arising from intermittent blade cavitation, loading, and thickness. *Trans. Soc. Naval Archit. Mar. Engrs* **90**, 111–151.

FABULA, A. G. 1962 Thin-airfoil theory applied to hydrofoils with a single finite cavity and arbitrary free streamline detachment. *J. Fluid Mech.* **12**, 227–240.

FINE, N. E. 1988 Computational and experimental investigations of the flow around cavitating hydrofoils. *Tech. Rep.* 88-6, MIT, Department of Ocean Engineering.

FINE, N. E. 1992 Nonlinear analysis of cavitating propellers in nonuniform flow. PhD thesis, Department of Ocean Engineering, MIT.

FINE, N. E. & KINNAS, S. A. 1992 A boundary element method for the analysis of the flow around 3-d cavitating hydrofoils. *J. Ship Res.* (to appear).

FRANC, J. P. & MICHEL, J. M. 1985 Attached cavitation and the boundary layer: experimental investigation and numerical treatment. *J. Fluid Mech.* **154**, 63–90.

FURUYA, O. 1975*a* Nonlinear calculation of arbitrarily shaped supercavitating hydrofoils near a free surface. *J. Fluid Mech.* **68**, 21–40.

FURUYA, O. 1975*b* Three-dimensional theory on supercavitating hydrofoils near a free surface. *J. Fluid Mech.* **71**, 339–359.

GEURST, J. A. & TIMMAN, R. 1956 Linearized theory of two-dimensional cavitational flow around a wing section. *IX Intl Cong. Applied Mech.*

LEMONNIER, H. & ROWE, A. 1988 Another approach in modelling cavitating flows. *J. Fluid Mech.* **195**, 557–580.

JIANG, C. W. & LEEHEY, P. 1977 A numerical method for determining forces and moments on supercavitating hydrofoils of finite span. In *Second Intl Conf. Numer. Ship Hydrodynamics, Berkeley, September*. National Academy Press.

KERWIN, J. E., KINNAS, S. A., LEE, J.-T. & SHIH, W.-Z. 1987 A surface panel method for the hydrodynamic analysis of ducted propellers. *Trans. Soc. Naval Archit. Mar. Engrs* **95**, 93–122.

KERWIN, J. E., KINNAS, S. A., WILSON, M. B. & MCHUGH, J. 1986 Experimental and analytical techniques for the study of unsteady propeller sheet cavitation. In *Proc. Sixteenth Symp. on Naval Hydrodynamics, Berkeley, California, July*, pp. 387–414. National Academy Press.

KINNAS, S. A. 1991 Leading-edge corrections to the linear theory of partially cavitating hydrofoils. *J. Ship Res.* **35**, 15–27.

KINNAS, S. A. & FINE, N. E. 1991 Non-linear analysis of the flow around partially or super-cavitating hydrofoils by a potential based panel method. In *Boundary Integral Methods-Theory and Applications, Proc. IABEM-90 Symp. Rome, Italy, October 15–19*, pp. 289–300. Springer.

KINNAS, S. A. & FINE, N. E. 1992 A nonlinear boundary element method for the analysis of unsteady propeller sheet cavitation. In *Proc. Nineteenth Symp. on Naval Hydrodynamics, Seoul, Korea, August 1992*. National Academy Press (in press).

KINNAS, S. A. & MAZEL, C. H. 1992 Numerical vs. experimental cavitation tunnel (a supercavitating hydrofoil experiment). In *Proc. 23rd American Towing Tank Conference, University of New Orleans, June 11–12, 1992*. National Academy Press (in press).

LEE, C.-S. 1979 Prediction of steady and unsteady performance of marine propellers with or without cavitation by numerical lifting surface theory. PhD thesis, MIT, Department of Ocean Engineering.

LEE, J.-T. 1987 A potential based panel method for the analysis of marine propellers in steady flow. PhD thesis, MIT, Department of Ocean Engineering.

LEEHEY, P. 1971 Supercavitating hydrofoil of finite span. In *IUTAM Symp. on Non-Steady Flow of Water at High Speeds, Leningrad, June 1971*, pp. 277–298.

MORINO, L. & KUO, C.-C. 1974 Subsonic potential aerodynamic for complex configurations: a general theory. *AIAA J.* **12**, 191–197.

NISHIYAMA, T. 1970 Lifting line theory of supercavitating hydrofoil of finite span. *Z. Angew. Math. Mech.* **50**, 645–653.

PELLONE, C. & ROWE, A. 1981 Supercavitating hydrofoils in non-linear theory. In *Third Intl Conf. on Numerical Ship Hydrodynamics, Basin d'essais des Carènes, Paris, France*. National Academy Press.

TULIN, M. P. 1953 Steady two-dimensional cavity flows about slender bodies. *Tech. Rep.* 834, David Taylor Model Basin.

TULIN, M. P. 1955 Supercavitating flow past foils and struts. In *Symp. on Cavitation in Hydrodynamics, NPL, Teddington, UK, September 1955*.

TULIN, M. P. 1964 Supercavitating flows – small perturbation theory. *J. Ship Res.* **7**, 16–37.

TULIN, M. P. & HSU, C. C. 1980 New applications of cavity flow theory. In *13th Symp. on Naval Hydrodynamics, Tokyo, Japan, 1980*. National Academy Press.

UHLMAN, J. S. 1978 A partially cavitated hydrofoil of finite span. *Trans. ASME* I: *J. Fluids Engng* **100**, 353–354.

UHLMAN, J. S. 1987 The surface singularity method applied to partially cavitating hydrofoils. *J. Ship Res.* **31**, 107–124.

UHLMAN, J. S. 1989 The surface singularity or boundary integral method applied to supercavitating hydrofoils. *J. Ship Res.* **33**, 16–20.

VAN HOUTEN, R. J. 1982 The numerical prediction of unsteady sheet cavitation on high aspect ratio hydrofoils. In *14th Symp. on Naval Hydrodynamics*. National Academy Press.

WIDNALL, S. E. 1966 Unsteady loads on supercavitating hydrofoils. *J. Ship Res.* **9**, 107–118.

WU, T. Y. & WANG, D. P. 1964 A wake model for free-streamline flow theory. Part 2. Cavity flow past obstacles of arbitrary profile. *J. Fluid Mech.* **18**, 65–93.